

교 과 목 414.519 강의록

수 치 선 박 유 체 역 학

- 보 텍 스 방 법 -

COMPUTATIONAL MARINE HYDRODYNAMICS
-VORTEX METHODS-

2019년 6월 27일

Suh, Jung - Chun

서 정 천

Seoul National Univ., Dept. NAOE

서울대학교 공과대학 조선해양공학과

7

FINITE VOLUME METHODS

7.1 Introduction	262
7.2 Numerical Implementation	263
7.2.1 Vorticity transport equation.	263
7.2.2 Biot-Savart integral	267
7.2.3 Pressure Poisson equation	270
7.2.4 Computational procedure.	272
7.3 Lid-driven Cavity Flows	275
7.3.1 Formulation	275
7.3.2 Comparison with analytic solution.	277
7.4 Impulsively Started Circular Cylinder.	281
7.4.1 General aspects	281
7.4.2 Computational grids	282

7.4.3 Numerical results	282
7.5 Oscillating Circular Cylinder Problems.	294
7.5.1 Key parameters	294
7.5.2 Flow characteristics.	295
7.5.3 Formulation for moving frame fixed to cylinder.	301
7.5.4 Numerical simulation.	302

7.1 Introduction

In this chapter, we focus on a vorticity-based integro-differential formulation for the numerical solution of the 2-D incompressible Navier-Stokes equations. A finite volume scheme is implemented to solve the vorticity transport equation with a vorticity boundary condition. The Biot-Savart integral is evaluated to compute the velocity field from a vorticity distribution over a fluid domain. The Green's scalar identity is employed to solve the total pressure in an integral approach. The global coupling between the vorticity and the pressure boundary conditions is considered when this integro-differential approach is employed. For the early stage development of the flow about an impulsively started circular cylinder, the computational results with our numerical method are compared with known analytical solutions in order to validate the present formulation.

A finite volume scheme is implemented to solve the vorticity transport equation with a vorticity boundary condition. The Biot-Savart integral is evaluated to compute the velocity field from a vorticity distribution over a fluid domain. The Green's scalar identity is employed to solve the total pressure in an integral approach. The global coupling between the vorticity and the pressure boundary conditions is considered when this integro-differential approach is employed. For the early stage development of the flow about an impulsively started circular cylinder, the computational results with our numerical method are compared with known analytical solutions in order to validate the present formulation.

We have mentioned in the previous chapter that the governing equations as well as the boundary conditions are globally coupled. The present method is im-

plemented in a time-stepping algorithm that proceeds by generating, convecting and diffusing the vorticity, by computing the corresponding velocity and by calculating the pressure with the vorticity and velocity field. Computationally, in order to recover the global coupling between the vorticity and the pressure for their discrete time-dependent solutions, two separate iterative procedures are required: one for solving the vorticity transport equation and the other for solving the total pressure equation.

7.2 Numerical Implementation

7.2.1 Vorticity transport equation

In solving the vorticity transport equation, we seek to advance the solution to the next time step with the velocity and the vorticity fields computed at the present time step. The vorticity field is then changed via the vorticity evolution mechanism.

The no-slip boundary condition is enforced in this stage by the production of a proper amount of vorticity at the body surface. This vorticity production is expressed in terms of the vorticity flux. The vorticity flux on the body surface is iteratively corrected until the no-slip condition is achieved within a preset criterion for the final vorticity field.

During the iteration, only the slip velocity is computed by the Biot-Savart integration, without computing the whole velocity field. The task is then to determine the vorticity distribution over a fluid domain at each instant in time, so that the no-slip condition is satisfied at the solid surface, the vorticity satisfies the vorticity transport equation, and the total vorticity of the field is conserved.

A finite volume discretization is applied to Eq. (6.42) which results in a consistent approximation to the conservation law, where the time rate of change of the vorticity within the domain is balanced by the net fluxes of the convective and the diffusive terms across the boundary surface of the domain. A physical domain is divided into a finite number of small elements, each element

serving as a computational cell. The vorticity field is considered as a discrete sum of the individual vorticity fields over the cells. The discretized solution to Eq. (6.42) results in a set of cell-averaged vorticity variables which is in balance with the face-averaged fluxes across the cell sides. Integrating the vorticity transport equation over an arbitrary but a stationary cell A with a cell boundary C and then applying the divergence theorem yields an integral form:

$$\frac{\partial}{\partial t} \int_A \omega dS + \oint_C \left((\underline{q} \cdot \underline{n}) \omega - \frac{1}{Re} \underline{n} \cdot \nabla \omega \right) dl = 0, \quad (7.1)$$

where $\left((\underline{q} \cdot \underline{n}) \omega - \frac{1}{Re} \underline{n} \cdot \nabla \omega \right)$ is the outward flux of ω across the cell boundary.

7.2.1.1 Numerical schemes

Let us assume that at the n th time step (corresponding to time t), the vorticity field has been computed (respecting the no-slip condition), then we seek to advance the solution to the $n + 1$ th time step (time $t + \Delta t$). We approximate Eq. (7.1) as a discrete integral form for both time and space coordinates, by replacing the boundary integral with the sum of the flux on the sides of the cell and using an explicit scheme in time-stepping:

$$\omega^{n+1} = \omega^n - \frac{\Delta t}{A} \sum_k F_k, \quad (7.2)$$

where ω^n is considered the average value of ω at the n th time stage over the cell whose area is A , and F_k represents the value of the flux outgoing through the k th side of the cell.

The diffusive flux term is approximated in its mean value sense in a similar fashion to the central differential scheme (Hoffman & Chiang 1993). For the convective term, the second-order TVD (total variation diminishing) scheme with the flux limiter suggested by Roe (1985) is used (see also Hirsch 1990). Time is advanced by an explicit forward Euler time stepping scheme during the time interval Δt . In fact, this is performed by several sub-steps with a smaller

time interval δt that satisfies the stability condition for this explicit scheme:

$$\delta t \leq \frac{d^2}{\frac{4}{Re} + \sqrt{2} q_s d}. \quad (7.3)$$

Here, d is the longer diagonal of a cell and q_s is the speed at the cell centroid. For global stability, we take actually a sub-step time increment smaller than the minimum value of such permissible values for all cells.

As the solution for the vorticity is advanced in time, the no-slip is presumably enforced at the beginning of each time increment. At the end of a time step, the distribution for ω would be changed eventually through the integration of Eq. (6.42). One must then calculate a new slip velocity at the surface. In order to reduce the slip velocity to zero, we require that the vorticity be produced at the surface acting as a source of vorticity (Lighthill 1963). The new vorticity would enter the fluid through the surface as represented by Eq. (6.48) and then would be allowed to diffuse and convect into the fluid over a finite time interval Δt . The task is to relate the vorticity flux on the surface of the body to this no-slip condition at the same time considering its coupling effect with the pressure.

7.2.1.2 No-slip boundary condition with vorticity flux

According to Eq. (6.47), vorticity is transferred to the fluid due to the tangential component of the pressure gradient and an acceleration of the body surface.

Wu et al. (1994) suggested that this pressure gradient is manifested by a spurious slip velocity observed on the body surface and this slip velocity is considered as an acceleration equivalent to a vorticity flux generated at the wall. The vortex sheet on the body surface should account for the modification of the circulation of the flow field.

$$\left(\nu \frac{\partial \omega}{\partial n} \right)^{(k+1)} = \left(\nu \frac{\partial \omega}{\partial n} \right)^{(k)} + \frac{V_s^{(k)}}{\Delta t} \quad (7.4)$$

where V_s is spurious slip velocity at the wall.

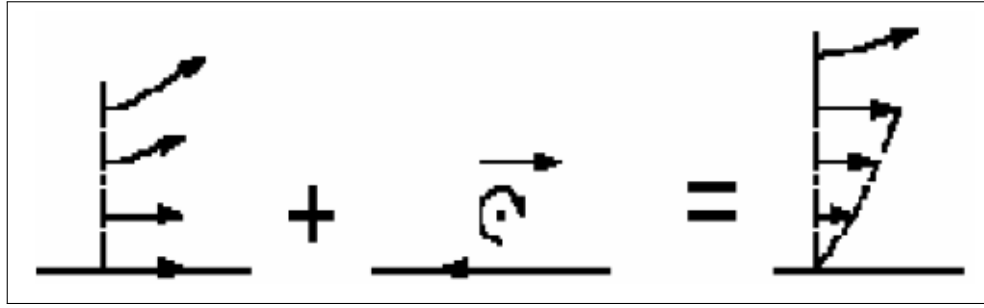


Figure 7.1 Iterative adjustment of vorticity flux for vorticity boundary condition. Adpated from Cottet & Poncet (2003).

In a discrete sense, the vorticity flux may be determined so that the no-slip condition is satisfied at the end of the time step. The spurious slip velocity (V_s) that would appear at the end of the time step can be regarded as the coupling term corresponding to the tangential gradient of the surface pressure in Eq. (6.48). The newly computed V_s can be then used to absorb the coupling term and consequently to update a time-averaged vorticity flux:

$$\bar{\sigma}^{(k+1)} = \bar{\sigma}^{(k)} + \frac{V_s^{(k)}}{\Delta t}, \quad (7.5)$$

where the overbar in $\bar{\sigma}$ denotes the time-averaged values of σ during a small time step Δt and the superscript notation refers to the iterative step. The iteration continues until the no-slip condition is satisfied, namely, until V_s reduces to a value within a preset allowance. Although there are practical considerations which must be observed during the specified time interval Δt , Eq. (7.5) implies that the integrated amount of vorticity flux is produced and remains unchanged during the time interval.

Now the vorticity (ω_b) at the body surface can be obtained from the definition of the vorticity flux, in a discrete differential sense,

$$\omega_b = Re d_1 \sigma + \omega_1, \quad (7.6)$$

where d_1 is the normal distance of the centroid of a cell adjacent to the body surface from the surface and ω_1 is the cell-centered vorticity value of the cell (see Figure 7.2).

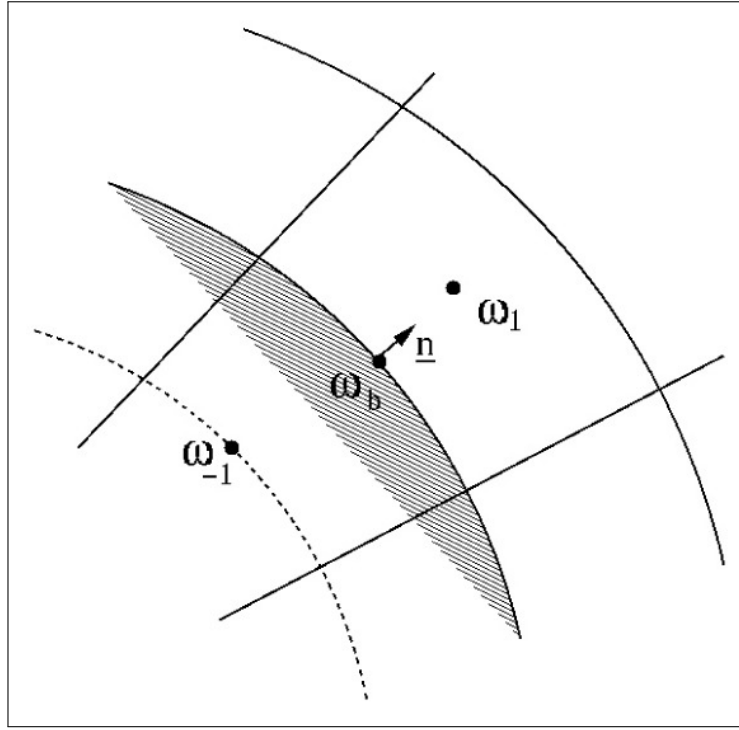


Figure 7.2 Notations for calculating the vorticity at the body surface.

7.2.2 Biot-Savart integral

In the vorticity-velocity integro-differential formulation, the Biot-Savart integral must be evaluated at appropriate field points within the discretized fluid domain. With N elements used in discretizing the fluid domain over which vorticity is distributed, we may require $O(N^2)$ evaluations of the Biot-Savart integral in order to calculate the velocity field. The evaluation of the Biot-Savart integral is, therefore, an important task in numerical implementations.

We will herein summarize the content described in Appendix D. See also Suh (2000) for the more detailed explanation and the extension of the present derivation to three-dimensions.

7.2.2.1 Evaluation of line integrals

The resulting expressions for the velocity field include the line integrals only along the boundary contour of the element. Let the value of the line integral

along each straight edge of the element be \underline{I}_i . Then, it follows that

$$\underline{u} = -\frac{k}{2\pi} \times \left(\sum_{i=1}^4 \underline{I}_i \right), \quad (7.7)$$

where the subscript i is denoted by the integer of the vertex associated with the first end point of the individual sides, ℓ_i denotes the length of i -th side and

$$\underline{I}_i = \frac{1}{2} \underline{n}_i \int_0^{\ell_i} \omega (\ln r^2 + 1) dl - \frac{1}{4} \nabla \omega (\underline{n}_i \cdot \underline{r}) \int_0^{\ell_i} \ln r^2 dl. \quad (7.8)$$

It is seen that the line integral for each side can be treated independently. After a substantial amount of algebraic manipulations, one may obtain the following result for \underline{I}_i :

$$\underline{I}_i = \frac{1}{2} \underline{n}_i \left\{ \omega_i \left(\ell_i + I^{(1)} \right) + (\nabla \omega \cdot \underline{s}_i) \left(\frac{1}{2} \ell_i^2 + I^{(2)} \right) \right\} - \frac{1}{4} \nabla \omega (\underline{n}_i \cdot \underline{r}) I^{(1)}, \quad (7.9)$$

where

$$\underline{r}_i = \underline{\xi}_i - \underline{x}, \quad x' = -\underline{r}_i \cdot \underline{s}_i, \quad y' = (\underline{r}_i \times \underline{s}_i) \cdot \underline{k}, \quad (7.10)$$

$$I^{(1)} = (\ell_i - x') \ln r_{i+1}^2 + x' \ln r_i^2 - 2\ell_i + 2|y'| \theta_i, \quad (7.11)$$

$$I^{(2)} = \frac{1}{2} (r_{i+1}^2 \ln r_{i+1}^2 - r_i^2 \ln r_i^2) - \frac{\ell_i^2}{2} + \ell_i x' + x' I^{(1)}, \quad (7.12)$$

and

$$\theta_i = \tan^{-1} \frac{|y'| \ell_i}{r_i^2 - \ell_i x'} \quad (\text{see Figure 7.3}) \quad (7.13)$$

7.2.2.2 Computational enhancement

Although this analysis deals with cases of linear distributions, the integration is much simpler, as a result of this construction, if ω is assumed to be constant over the cell. The actual numerical implementation in the present work is performed under the assumption that the vorticity density is piecewise uniform over discretized cell elements of a fluid domain.

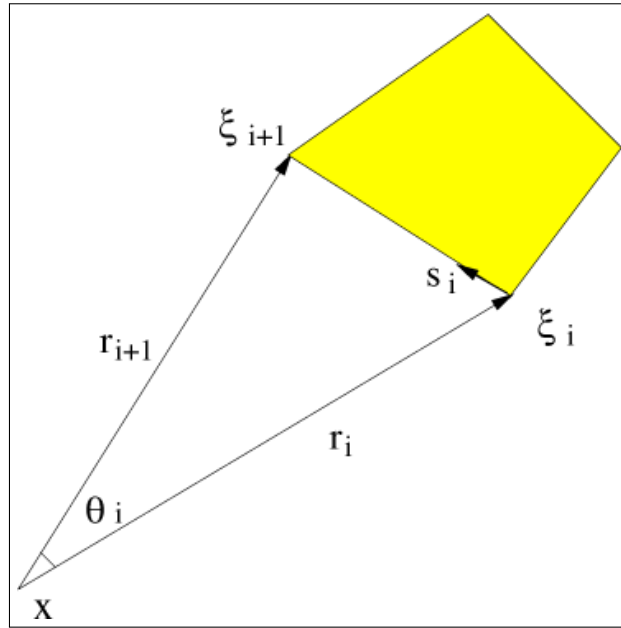


Figure 7.3 Notations for the contour integral of the quadrilateral element. Here, ω_i denotes the vorticity value at the i -th vertex, s_i is the unit directional vector of the line integral path, and we denote the distances between the two end points of the side and the field point by r_i and r_{i+1} , respectively.

The present procedure is believed to be quite accurate, but it is nevertheless time-consuming to apply computationally because of a few of the transcendental functions involved in closed-forms. In the present numerical implementation, therefore, for a vorticity distribution with unit density over each cell element, we compute once the induced velocities at desired field points (namely, at centroids of neighboring cell elements) and then save them (within the limit of computer memory capacity) so that such time-consuming calculations can be avoided. Furthermore, when the distance r is sufficiently large (say, more than five times the diagonal dimension of the fluid element), Eq. (6.43) is applied directly without such integrations. That is, the vorticity within the region of area A is treated as a point vortex of strength ωA located at the centroid of the element. The sum of all of the induced velocities from the vorticity is then added to the contribution from the onset flow. In this manner, we can calculate the whole velocity field as well as the slip velocity at the surface.

7.2.3 Pressure Poisson equation

7.2.3.1 Formulation

Once the vorticity and the velocity field are updated, the integral equation for the total pressure must be solved to provide a complete set of solutions at the $n + 1$ th time step. Substituting Eq. (6.49) for $\frac{\partial H}{\partial n}$ into Eq. (6.44) yields the limiting form for H as a field point approaches the surface points (\underline{x}_B) of a solid body:

$$\begin{aligned} \frac{1}{2}H + \frac{1}{2\pi} \oint_{C_B} H \frac{\partial(\ln r)}{\partial n} dl = \\ -\frac{1}{2\pi} \oint_{C_B} \left[\underline{n} \cdot \frac{\partial \underline{q}}{\partial t} - \underline{n} \cdot (\underline{q} \times \underline{\omega}) + \frac{1}{Re} \underline{n} \cdot (\nabla \times \underline{\omega}) \right] \ln r dl \\ + \frac{1}{2\pi} \int_S \nabla \cdot (\underline{q} \times \underline{\omega}) \ln r dS, \end{aligned} \quad (7.14)$$

where the integrals over C_B is evaluated on the surface of a body in the sense of the Cauchy principal value integral. Using the vector operation for the integrand of the surface integral in Eq. (7.14), namely, $\nabla \cdot (\underline{q} \times \underline{\omega}) \ln r = \nabla \cdot (\underline{q} \times \underline{\omega} \ln r) - (\underline{q} \times \underline{\omega}) \cdot \nabla(\ln r)$ and applying the divergence integral theorem to the resultant expression, yield a Fredholm integral equation of the second kind for H :

$$\begin{aligned} \frac{1}{2}H + \frac{1}{2\pi} \oint_{C_B} H \frac{\partial(\ln r)}{\partial n} dl = -\frac{1}{2\pi} \oint_{C_B} \left[\underline{n} \cdot \frac{\partial \underline{q}}{\partial t} + \frac{1}{Re} \underline{n} \cdot (\nabla \times \underline{\omega}) \right] \ln r dl \\ - \frac{1}{2\pi} \int_S (\underline{q} \times \underline{\omega}) \cdot \nabla(\ln r) dS. \end{aligned} \quad (7.15)$$

Furthermore, if we assume the body to be either fixed or impulsively started as in our test problem later on, the equation reduces to a simpler one:

$$\begin{aligned} \frac{1}{2}H + \frac{1}{2\pi} \oint_{C_B} H \frac{\partial(\ln r)}{\partial n} dl = -\frac{1}{2\pi} \oint_{C_B} \frac{1}{Re} \frac{\partial \omega_B}{\partial s} \ln r dl \\ - \frac{1}{2\pi} \int_S (\underline{q} \times \underline{\omega}) \cdot \nabla(\ln r) dS. \end{aligned} \quad (7.16)$$

7.2.3.2 Application of panel methods

Accordingly, we base our pressure calculation on an integral equation formation of the pressure-Poisson equation. One possible approach for solving Eq. (7.16) numerically for the total pressure is to use a panel-method approximation in a similar fashion to a one in potential flow analysis. Among the full variety of the numerical implementation of the panel methods, we use herein a straight-line element for the body contour subdivision representation, and a uniform density distribution of singularity strength on each panel at the boundary and over each cell in the fluid domain. This low-order panel-method approximation is relatively robust in the numerical implementation and thus the computing time can be reduced in comparison with other higher-order panel methods without significant loss of accuracy in numerical results.

The body is defined by a set of points on the surface and the body surface is subdivided into N (normally an even number) straight-line elements (flat panels or interior facets). This approximate representation for the body surface enables us to replace the two integrals over C_B in Eq. (7.16) by the sum of the individual integral form for the contribution of each straight-line panel.

The surface integral term on the right-hand side of Eq. (7.16) is similar in form to the Biot-Savart integral in Eq. (6.43) if we replace $(\underline{q} \times \underline{\omega}) \cdot \nabla(\ln r)$ by $\underline{\omega} \times \nabla(\ln r)$. In order to include the influence of the field distribution of $(\underline{q} \times \underline{\omega})$, we can use the algorithm for evaluation of the Biot-Savart integral described in Section 3.2 under the assumption that the distribution is piecewisely constant over each cell element.

Although we have already used the pressure boundary condition Eq. (6.49) when we derived Eq. (7.16), the term $-\frac{1}{Re} \frac{\partial \omega_B}{\partial s}$ must be evaluated in order to actually impose the boundary condition on the equation. At this stage, we need the iteration procedure to specify the value, which will be described later on.

Consequently Eq. (7.16) deduces a set of algebraic expressions with unknown values of the total pressure head ($H_i, i = 1, \dots, N$) on the panels. With H_i being solutions of this linear system, the total pressure field can be obtained by integrating Eq. (7.16). The pressure field, as well as the surface

pressure distribution, can be determined by subtracting the dynamic pressure term in Eq. (6.27) from the total pressure.

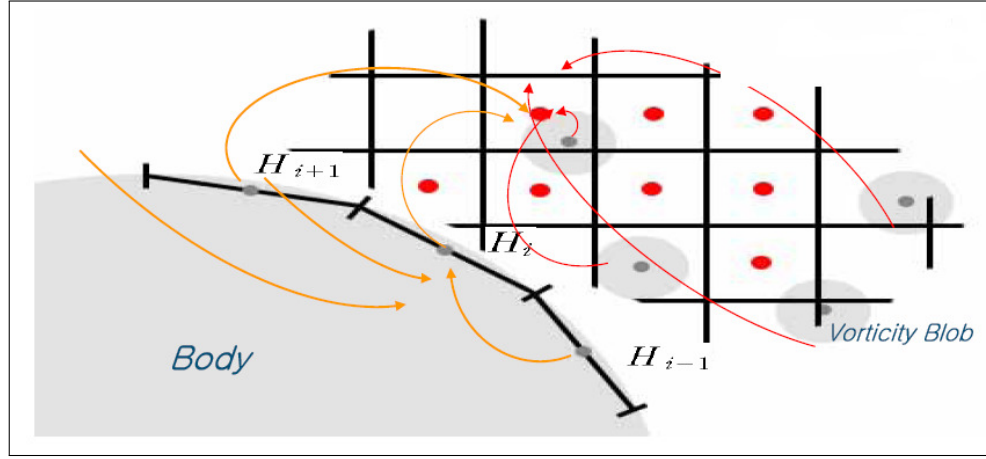


Figure 7.4 Schematic diagram for calculation of pressure field.

7.2.4 Computational procedure

The above considerations can be summarized in the following algorithm of the solution of a system of the governing equations.

- (1) Integrate the vorticity transport equation, Eq. (6.42), in time with enforcement of the no-slip condition. At the n th time step (corresponding to time t) the velocity and the vorticity fields are assumed to be computed and we seek to advance the solution to the $n + 1$ time step (time $t + \Delta t$). Given \underline{q}^n and ω^n , the vorticity field ω^{n+1} at the $n + 1$ th time step is changed via the vorticity evolution mechanism. The no-slip boundary condition is enforced in this stage by assigning the vorticity flux at the solid surface. The vorticity flux at the surface is assigned as its time-averaged value during a small time interval as given by Eq. (7.5). We need an iterative process to introduce a proper amount of the time-averaged vorticity flux in order to ensure the no-slip condition and accordingly update ω^{n+1} . The spurious slip velocity is computed by performing the Biot-Savart integration for the vorticity field obtained at the present iterative stage.
- (2) Evaluate the Biot-Savart integral by using the integration scheme proposed in Section 7.2.2 in order to obtain the velocity field \underline{q}^{n+1} corresponding to

the currently updated vorticity field ω^{n+1} . The vorticity is assumed to be distributed with a uniform strength over an individual cell element. Since the job of the Biot-Savart integration is repeated for all time steps, it is desirable to save computing time by storing the results of the Biot-Savart integral for a unit vorticity-distribution over an individual cell. Because of limited storage in a computer, it applies for field points within a certain distance away from the cell for which we use the exact integration.

- (3) Solve the integral equation for H^{n+1} by using \underline{q}^{n+1} and ω^{n+1} obtained in steps (1) and (2). The term $-\frac{1}{Re} \frac{\partial \omega_B}{\partial s}$ in Eq. (7.16) must be evaluated where the differentiation performs in the direction s tangent to the surface of the body. To obtain the vorticity (ω_B) at the body surface given by Eq. (7.6), the vorticity flux must be evaluated in this stage at the end of the time interval while in step (1), the rate of vorticity production was taken to be uniform over the time t to $t + \Delta t$.

Since the vorticity flux is related to the tangential gradient of the pressure along the body surface and the normal gradient of the total pressure is incorporated with the tangential gradient of the body vorticity at the current time, we employ the iterative calculation between the vorticity flux and the pressure on the surface. With the time-averaged vorticity flux obtained in step (1), we obtain the body vorticity via Eq. (7.6). Then we use this body vorticity value as an initial guess and \underline{q}^{n+1} and ω^{n+1} in order to solve Eq. (7.16) for H and thus to find the pressure at the surface. The tangential gradient of this surface pressure is used to update the vorticity flux at the $(n + 1)$ th time step by Eq. (6.48). With this updated vorticity flux at the end of a time step, we update the body vorticity via Eq. (7.6) again.

This iterative procedure is continued until the surface pressure and the vorticity flux reach a converged state. The convergence of the iteration process is measured with the difference in their values between two successive iterations. The typical tolerance is taken as 10^{-4} in our test problem later on. Up to this point, the principle of conservation of vorticity can be invoked by integrating Eq. (6.48).

When the pressure gradient is then integrated around the closed contour of

the a solid body, the result must be zero because the pressure is inherently a single-valued function. It is the argument leading to the principle of the vorticity conservation that the total vorticity in the infinite unlimited space occupied jointly by the fluid and the solid bodies is always zero.

- (4) Advance the calculation to the next time step by repeating steps (1), (2) and (3).

The reconstruction of the surrounding cell-averaged data to a common vertex or node is performed by a weighted averaging procedure based on an inverse-distance weighted averaging of the variables from the cell centroid to the cell vertices.

The above solution procedure is summarized in Figure 7.5 .

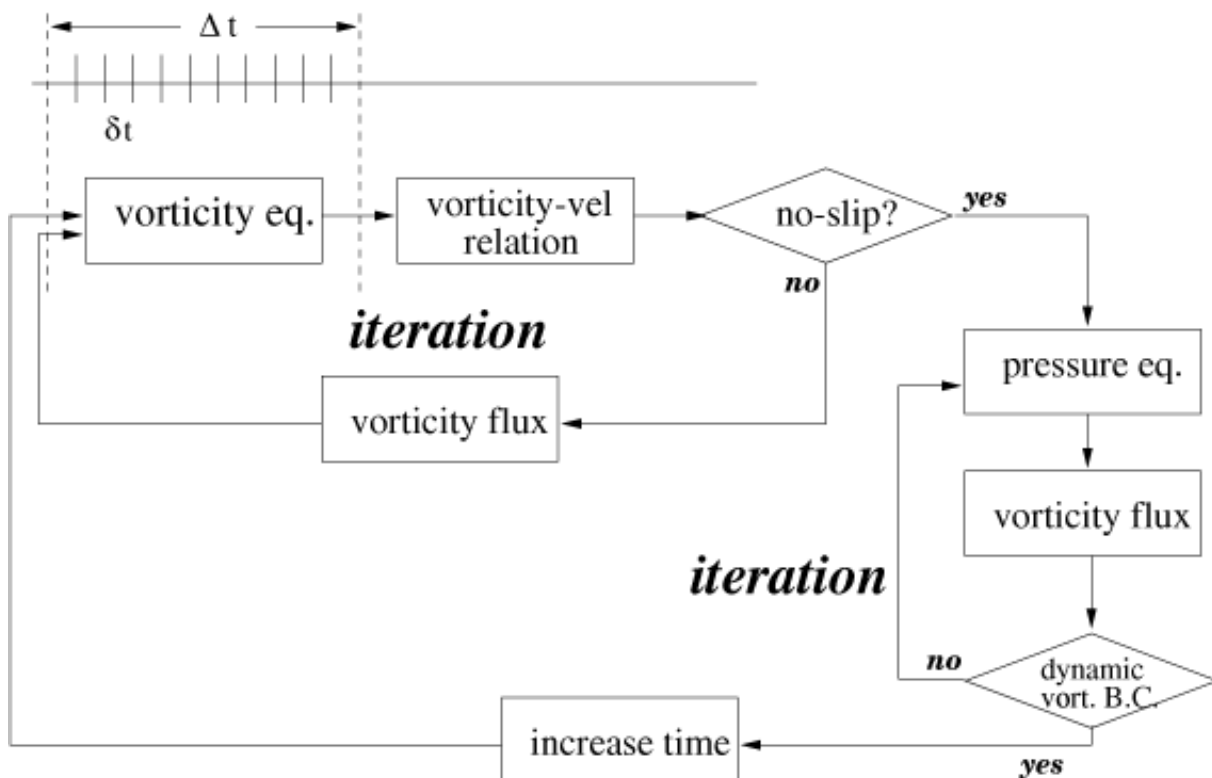


Figure 7.5 Flow chart for solution procedure of the present FVM in the vorticity-velocity-pressure formulation.

7.3 Lid-driven Cavity Flows

7.3.1 Formulation

As an application of the present scheme, we consider a vorticity-based integro-differential formulation for the numerical solution of a two dimensional cavity flow driven by shear and body forces (see Figure 7.6) (Rida et al. 1997, Shih et al. 1989).

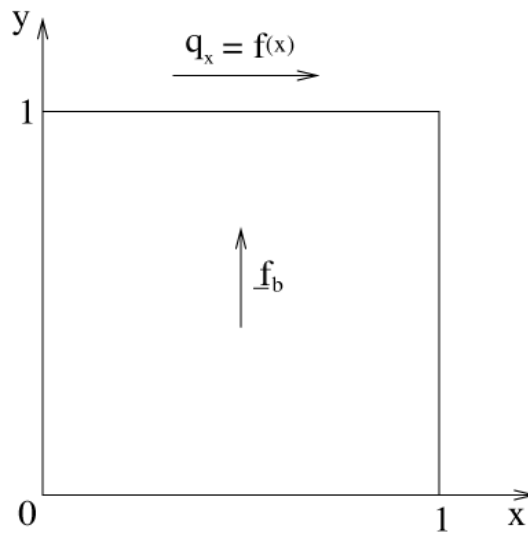


Figure 7.6 Coordinates and geometry for driven cavity.

The shear motion of the lid of the cavity and the body force are prescribed as, respectively,

$$f(x) = x^4 - 2x^3 + x^2 \quad (7.17)$$

$$\underline{f}_b = 8\mu [24 F(x) + 2f'(x) g''(y) + f''' g(y)] \underline{j} + 64 [F_2(x) G_1(y) - g(y) g'(y) F_1(x)] \underline{j}, \quad (7.18)$$

where

$$g(y) = y^4 - y^2, \quad F(x) = \int_0^x f(x) dx, \quad F_1(x) = f(x) f''(x) - [f'(x)]^2, \\ F_2(x) = 0.5 f^2(x), \quad G_1(y) = g(y) g'''(y) - g'(y) g''(y). \quad (7.19)$$

This lid-driven square cavity flow is a standard benchmark for testing numerical

schemes in the context of computational fluid dynamics because of its simplicity and the availability of the analytical solution.

The governing equations for the unsteady flow of an incompressible Newtonian fluid can be written as,

$$\nabla \cdot \underline{q} = 0, \quad (7.20)$$

$$\underline{\omega} = \nabla \times \underline{q}, \quad (7.21)$$

$$\frac{\partial \underline{\omega}}{\partial t} + \underline{q} \cdot \nabla \underline{\omega} = \underline{\omega} \cdot \nabla \underline{q} + \nu \nabla^2 \underline{\omega} + \nabla \times \underline{f}_b, \quad (7.22)$$

$$\nabla^2 \left(\frac{p}{\rho} + \frac{1}{2} q^2 \right) = \nabla \cdot \left(\underline{q} \times \underline{\omega} + \underline{f}_b \right), \quad (7.23)$$

The corresponding integro-differential vorticity-velocity formulation is given, in non-dimensional form, by,

$$\frac{\partial \omega}{\partial t} + \nabla \cdot (\underline{q} \omega) = \frac{1}{Re} \nabla^2 \omega + \nabla \times \underline{f}_b, \quad (7.24)$$

$$\underline{q} = \underline{q}_o - \frac{1}{2\pi} \int_S \underline{\omega} \times \nabla (\ln r) dS, \quad (7.25)$$

$$\begin{aligned} H = & -\frac{1}{2\pi} \oint_C \left[H \frac{\partial (\ln r)}{\partial n} - \frac{\partial H}{\partial n} \ln r \right] dl \\ & + \frac{1}{2\pi} \int_S \nabla \cdot \left(\underline{q} \times \underline{\omega} + \underline{f}_b \right) \ln r dS, \end{aligned} \quad (7.26)$$

where p is the pressure, ν the kinematic viscosity, ρ the density of the fluid, Re the Reynolds number and ω the scalar plane component of the vorticity vector ($\underline{\omega} \equiv \omega \underline{k}$). The velocity term \underline{q}_o in Eq. (7.25) represents the contribution from the velocity distributions over the boundary(C) of the cavity, namely:

$$\underline{q}_o = \oint_C \left[(\underline{n} \cdot \underline{q}) \nabla G + (\underline{n} \times \underline{q}) \times \nabla G \right] dl, \quad (7.27)$$

where \underline{n} is the unit normal pointing into the fluid at the boundary C . The pres-

sure p is related to the total pressure defined by

$$H = \frac{p - p_r}{\rho} + \frac{1}{2} (q^2 - q_r^2), \quad (7.28)$$

where the constants p_r and q_r are the reference pressure and velocity, respectively. In such a formulation, we deal with the Biot-Savart integral in order to compute the velocity from a vorticity distribution in the square cavity and to solve the total pressure in a boundary integral approach.

The boundary conditions for the velocity, the vorticity and the pressure supplement the system of Eqs. (7.24), (7.25) and (7.26). The no-slip velocity condition states that the velocity of the fluid (\underline{q}) is equal to the moving velocity (\underline{U}_B) of the boundary (\underline{x}_B) of the cavity:

$$\underline{q}(\underline{x}_B, t) = \underline{U}_B \quad \text{on } C. \quad (7.29)$$

The boundary condition for the vorticity flux (σ) at the boundary can be derived by taking the cross product of the Navier-Stokes equations with \underline{n} and by using the velocity adherence condition:

$$\sigma \equiv -\frac{1}{Re} \frac{\partial \omega}{\partial n} = -\underline{k} \cdot \underline{n} \times \left(\frac{d\underline{U}_B}{dt} + \nabla p - \underline{f}_b \right) \quad \text{on } C. \quad (7.30)$$

Similarly, the scalar product of the Navier-Stokes equations with \underline{n} gives an expression for $\partial H / \partial n$ as:

$$\frac{\partial H}{\partial n} = -\underline{n} \cdot \left(\frac{\partial \underline{q}}{\partial t} - \underline{q} \times \underline{\omega} + \frac{1}{Re} \nabla \times \underline{\omega} - \underline{f}_b \right) \quad \text{on } C. \quad (7.31)$$

7.3.2 Comparison with analytic solution

For purposes of comparison with the exact steady-state solution, the calculations are advanced to steady-state. As the initial condition in the time evolution of the flow, an impulsive start was formulated. A uniform grid of equal size that divides the cavity flow region was used. The vorticity, the vorticity flux, and the pressure distributions along the cavity wall for $Re = 100$ with variation of the

time interval and the grids are shown in Figs. 7.7 and 7.8 , where the agreement with the exact solution is excellent.

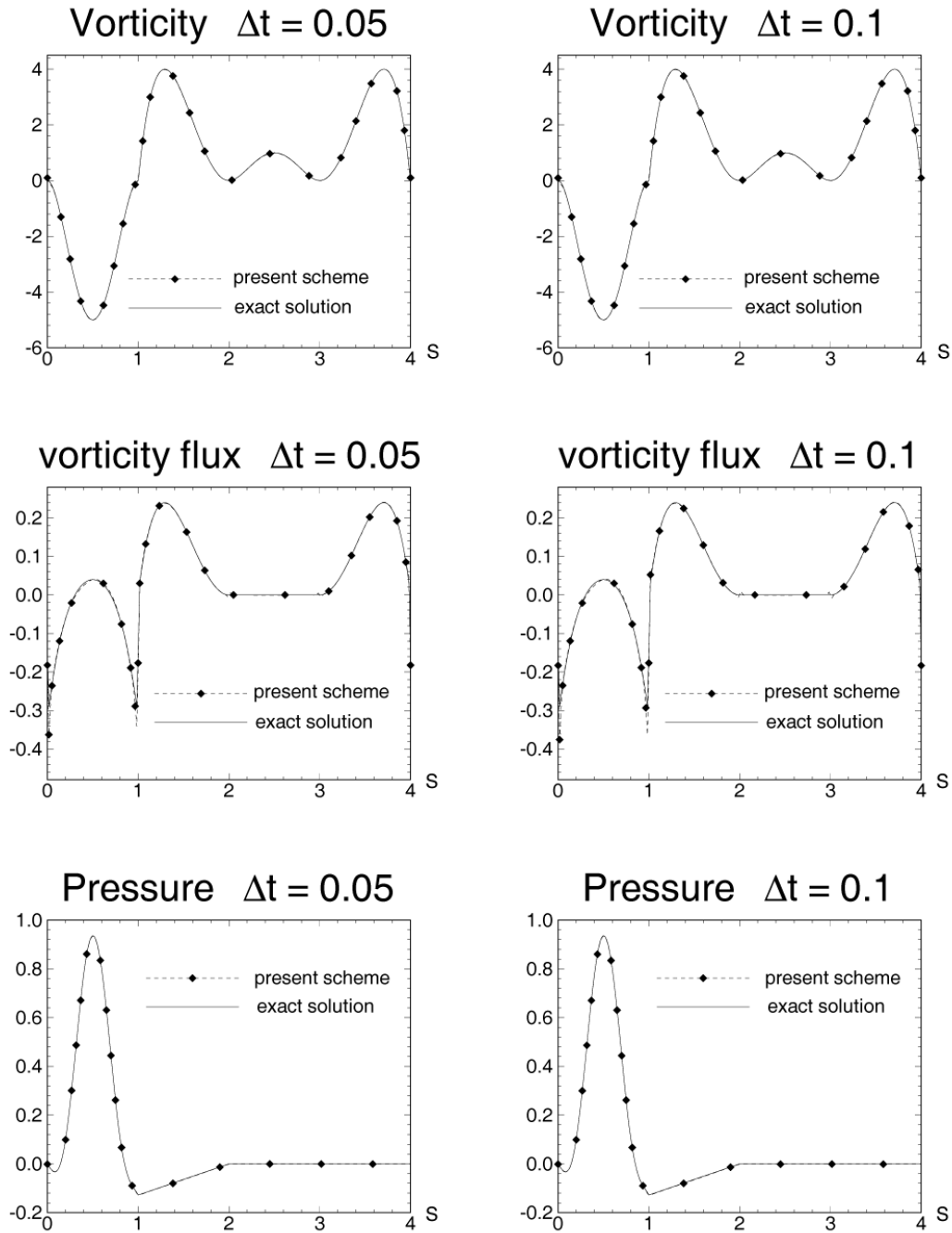


Figure 7.7 Sensitivity of time interval on vorticity, vorticity flux and pressure along the driven cavity wall for $Re = 100$ with the 61×61 grid. The perimeter(S) along the cavity wall has the clockwise direction from the origin at the upper left corner of the cavity.

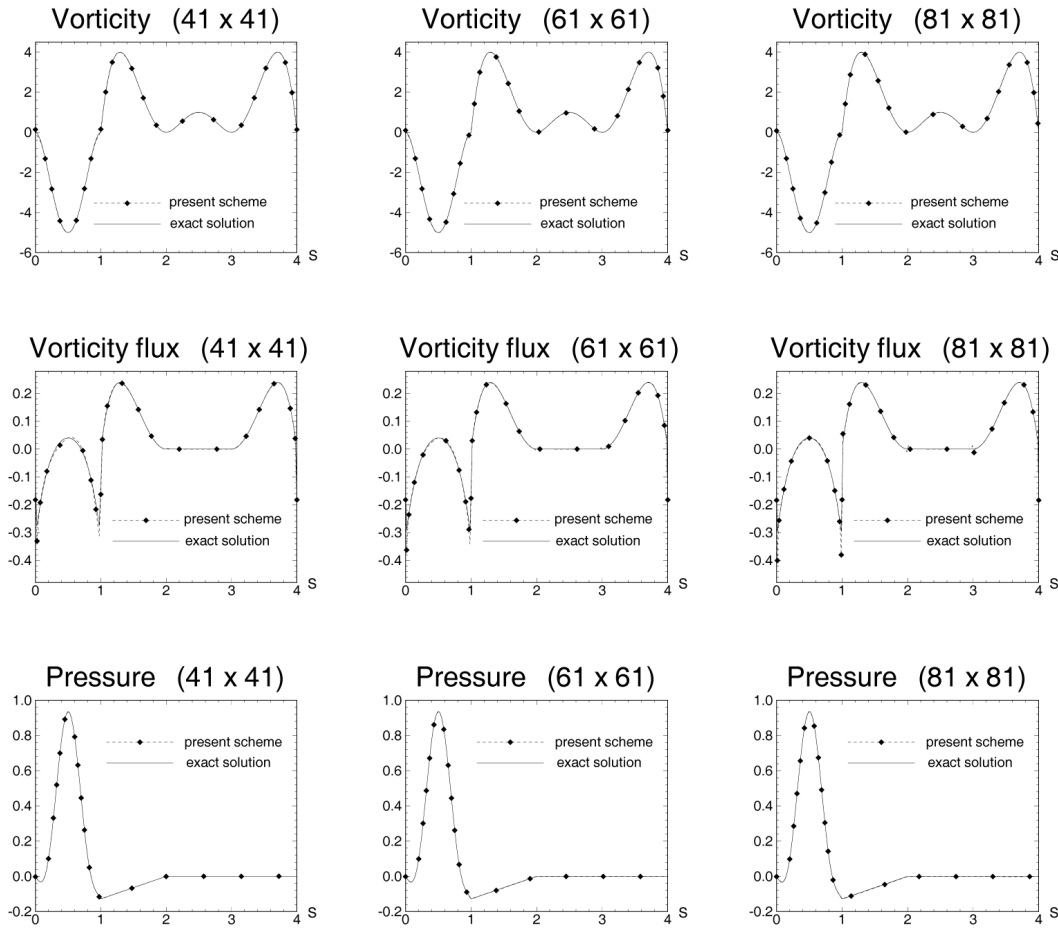


Figure 7.8 Sensitivity of mesh size on vorticity, vorticity flux and pressure along the driven cavity wall for $Re = 100$ with $\Delta t = 0.05$.

Figure 7.9 shows that the time evolution of the velocity along the vertical and the horizontal center lines of the cavity at $Re = 100$ with $\Delta t = 0.05$ and the 61×61 grid. Figure 7.10 shows the time evolution of kinetic energy for cavity flow in this case. This is compared with the exact steady-state value $1216/33075 (= 0.0367650)$. The streamline pattern, the vorticity contour, and the pressure contour in the steady-state are shown in Figure 7.11, where the agreement is again very good. (It is difficult to distinguish between the exact solution and the numerical solution with the present scheme.)

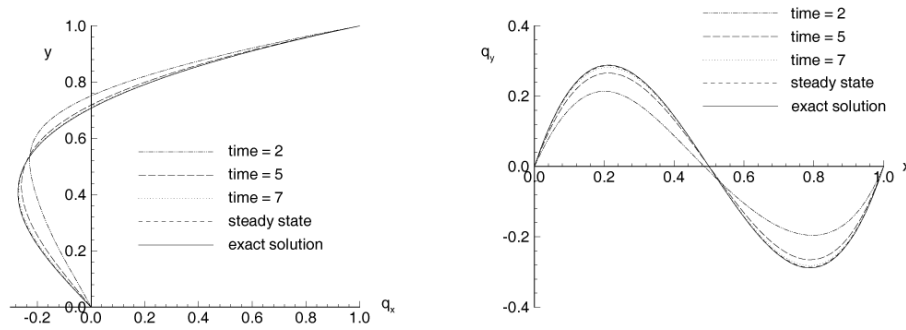


Figure 7.9 Time evolution of the velocity along the center lines of the driven cavity for $Re = 100$ with $\Delta t = 0.05$ and the 61×61 grid.

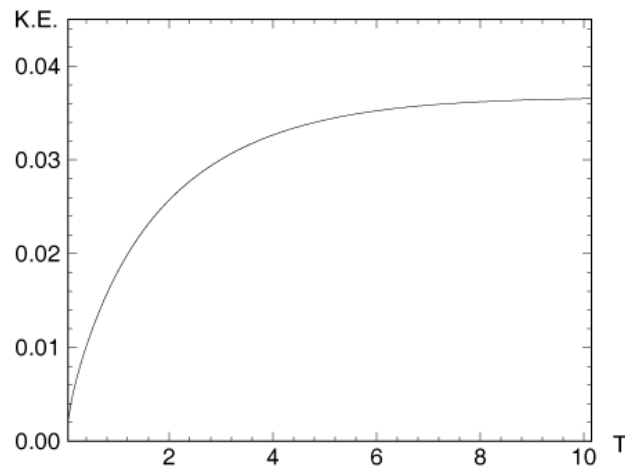


Figure 7.10 Time evolution of kinetic energy of the driven cavity for $Re = 100$ with $\Delta t = 0.05$, and the 61×61 grid.

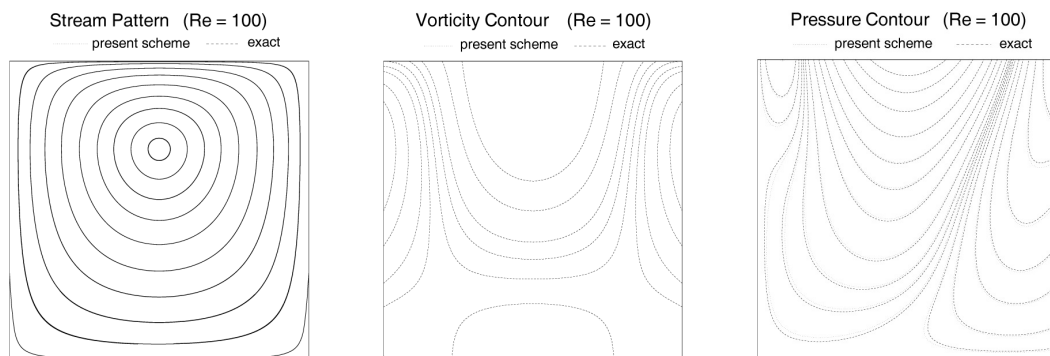


Figure 7.11 Streamline pattern, vorticity contour and pressure contour of the driven cavity for $Re = 100$ with $\Delta t = 0.05$ and the 61×61 grid.

The above comparison implies that the evaluation of the Biot-Savart integral works well. In the present numerical implementation, for a vorticity distribution with unit density over each cell element, we compute the induced velocities at desired field points once (namely, at centroids of neighboring cell elements) and then save them (within the limit of computer memory capacity) so that the time-consuming calculations at successive time steps can be avoided.

7.4 Impulsively Started Circular Cylinder

7.4.1 General aspects

As a numerical example we consider the case of an impulsively started circular cylinder at certain Reynolds numbers. The numerical simulation for the development of two-dimensional, incompressible flow past an impulsively started circular cylinder has been a challenge to computational fluid dynamicists for years. Although the geometry is simple, the flow pattern in the proximity of the circular cylinder is in full variety. Treatment of these special flow problems requires complex numerical procedures to be applied and often validation is defined by comparisons with analytical solutions.

A notable theoretical investigation of the initial flow over an impulsively started circular cylinder was given by Bar-Lev & Yang (1975). They solved the vorticity transport equation by the method of matched asymptotic expansions to the third order of a small quantity of non-dimensional time. Their analytical solution would be reasonably valid for $t < 0.25$, $Re > 50$. Only for the purpose of comparison with the analytical solution, no attempt is made to advance the calculations to large time values. Rather, the intent is only to provide sufficient results in the early time stage after the impulsive start, from which the validity of the present formulation can be demonstrated. Our calculations are concentrated on those of the vorticity and vorticity flux distribution, the pressure distribution and the drag coefficient.

As the initial condition in the evolution of the flow, an impulsive start may be formulated using the potential flow field although there cannot experimentally

be such a thing as a truly impulsive start. At time $t = 0^+$ the slip velocity distribution ($2 \sin \theta$) obtained from the potential flow analysis is imposed on the surface of the body. In fact, numerical schemes encounter difficulties in resolving the initially developed thin boundary layers associated with impulsive starts. There exists inherently the singular behavior (having infinity value) on the (drag) force at the time immediately after the impulsive start.

7.4.2 Computational grids

An O-type regular pattern of quadrilateral cells that divides the fluid region about a circular cylinder is used, but we believe a C-type grid will work as well. Our computational domain is described by a set of grid points taken as $\theta_i = 2\pi i/N_I$ and $r_j = R_o - (R_o - 0.5) \cos(\pi j/2N_J)$, where N_I is the number of cells in the circumferential direction, N_J in the radial direction and R_o is the outer radius of the boundary of the computational domain. Since the first i -index coincides with the last i -index, a periodic boundary condition is applied along the interface corresponding to that index. On the cylinder surface ($r = 0.5$) which corresponds to $j = 1$, we set the vorticity flux (vorticity production) to a suitable value determined iteratively from the no-slip boundary condition. On the outer boundary, we convect purely ω out of the computational domain in a naturally upwind sense (i.e., without the diffusion term in Eq. (7.2), $\omega^{n+1} = \omega^n - \frac{\Delta t}{A} \sum_k \{(\underline{q} \cdot \underline{n}) \omega^n\}_k$.

7.4.3 Numerical results

7.4.3.1 Analytic solution in early time stage

In Figures. 7.12 through 7.14, the effect of numerical parameters on the pressure drag, the friction drag and the total drag coefficients as computed by the present method is presented for Reynolds number $Re = 60, 3000$ and 9500 . The analytical solutions given by Bar-Lev and Yang (1975) are also presented

for the purpose of comparison. The frictional and the pressure drag were calculated by integrating the vorticity and the pressure, respectively, over the surface of the cylinder. The drag coefficients are normalized by $\frac{1}{2} \rho q_\infty^2 D$.

7.4.3.2 Time step

In Figure 7.12 we plot the sensitivity of the time interval Δt on the drag for each Reynolds number. For the convergence check, three different time intervals ($\Delta t = 0.0025, 0.005, 0.01$) have been chosen. The grid used in these calculations was 600×80 and the outer radius of the computational domain was taken as $R_o = 1.5$. The present results are shown to give good convergence with respect to Δt to the analytical solutions, especially near the immediate time region (near $t = 0^+$) after impulsive start. The inherently singular behavior of the solution is precisely captured as Δt becomes smaller. We observe that the numerical results are in good agreement with the analytical solutions for $t < 0.25$, even when using a moderate time interval of $\Delta t = 0.01$.

7.4.3.3 Computational domain

In Figure 7.13 the effect of the size of the computational domain on the drag is presented. Note that it is difficult to make distinctions between all the symbols in the figures. It seems that the effect is negligible if the computational domain contains entirely the fluid domain with non-zero vorticity values like the present cases. But it is apparent that, as time advances, the computational domain should become larger in order to contain the region with non-zero vorticity values.

Figure 7.14 shows the corresponding effect with respect to a measure of the mesh size. We see that the grid dependence on the solutions is small enough to ignore unless grid resolutions for capturing a complicated vortex structure are required. At the early stage in time for the present cases, the complicated vortex structure is not exhibited yet. In the following computations, $\Delta t = 0.005$, the 600×80 grid, and $R_o = 1.5$ are used, from the viewpoint that these choices would not greatly affect our numerical results.

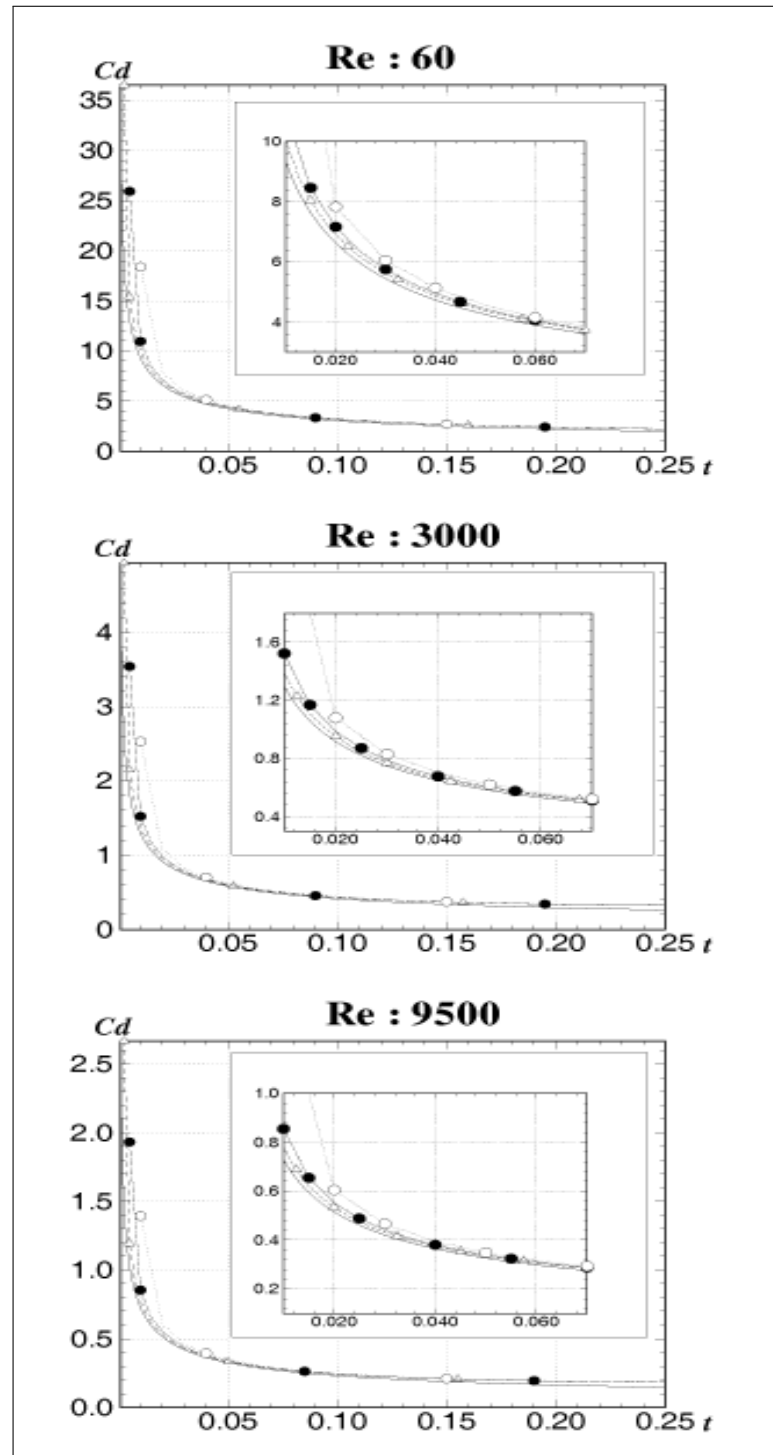


Figure 7.12 Sensitivity of the time interval on the drag coefficients of the impulsively started circular cylinder at $Re = 60, 3000$ and 9500 with $R_o = 1.5$ and the 600×80 grid.
 —, analytical (Bar-Lev & Yang (1975)); \triangle , $\Delta t = 0.0025$; \bullet , $\Delta t = 0.005$; \circ , $\Delta t = 0.01$

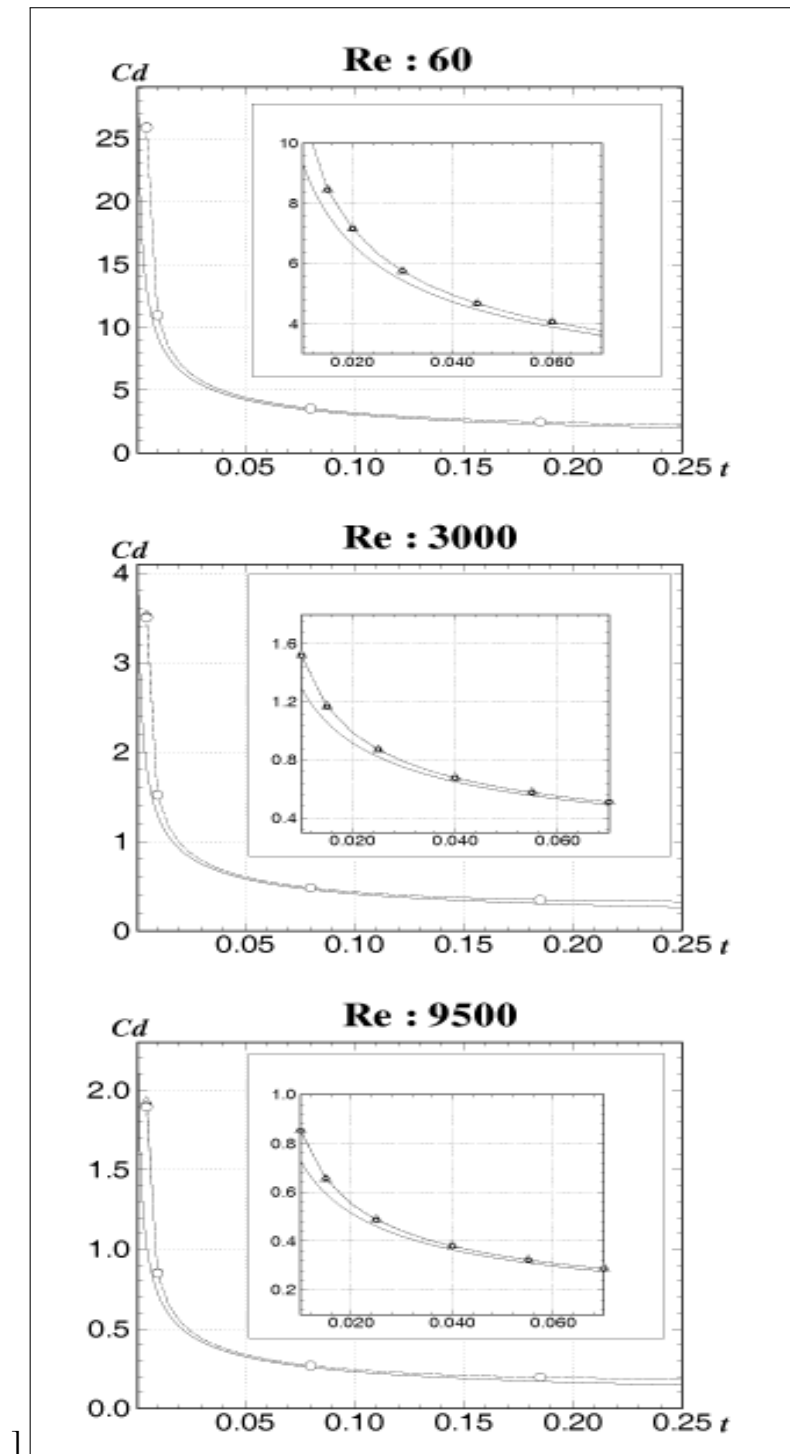


Figure 7.13 Sensitivity of the outer radius on the drag coefficients of the impulsively started circular cylinder at $Re = 60, 3000$ and 9500 with $\Delta t = 0.005$ and the 600×80 grid.

—, analytical (Bar-Lev & Yang (1975)); \triangle , $R_o = 1.5$; \bullet , $R_o = 2.5$; \circ , $R_o = 3.5$

Note: The results corresponding to $R_o = 2.5$ are not detectable because of the nearly same values as the others.

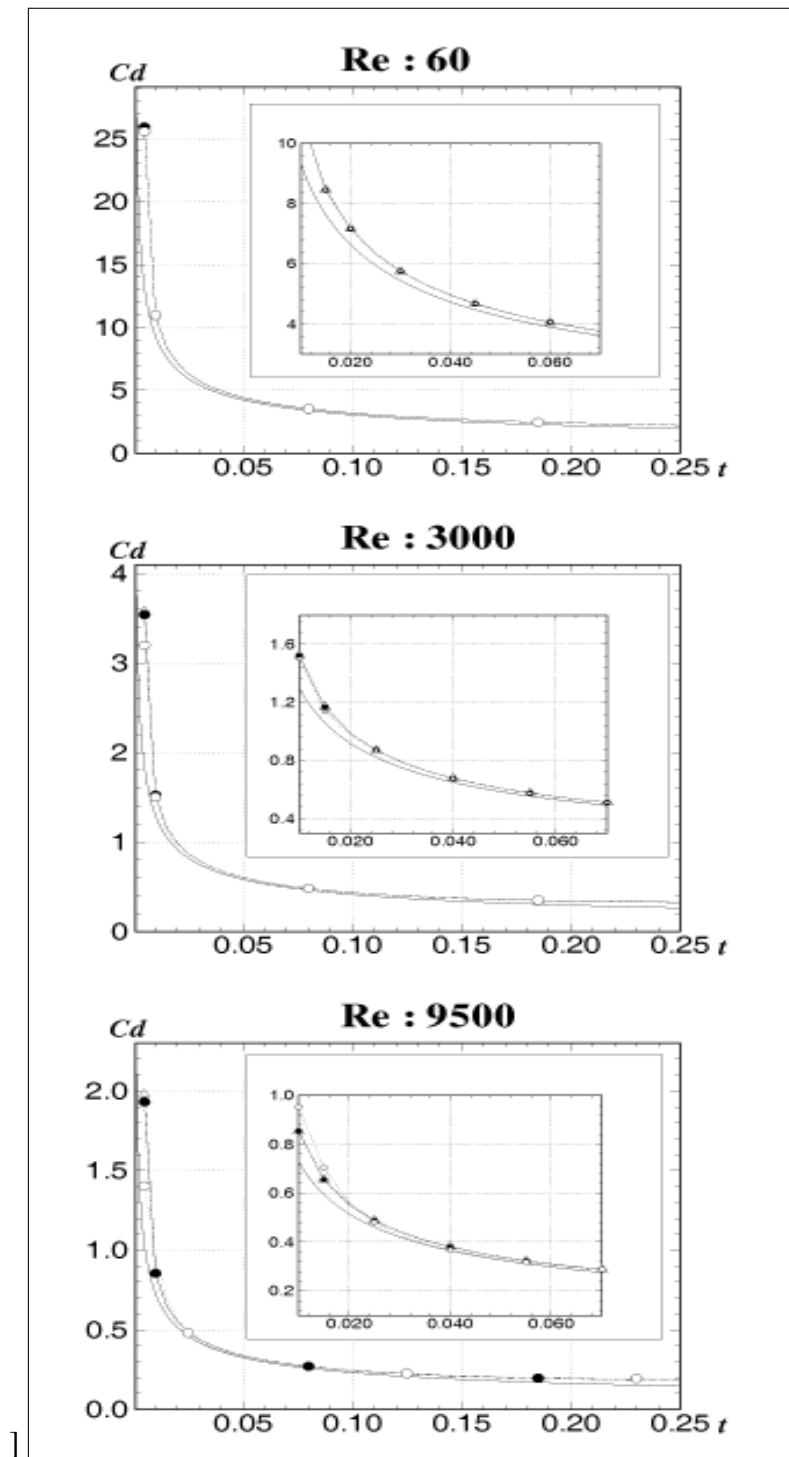


Figure 7.14 Sensitivity of the mesh size on the drag coefficients of the impulsively started circular cylinder at $Re = 60, 3000$ and 9500 with $\Delta t = 0.005$ and $R_o = 1.5$.
 —, analytical (Bar-Lev & Yang (1975)); Δ , grid 800×100 ; \bullet , grid 600×80 ; \circ , grid 300×40

7.4.3.4 Reynolds number

In Figure 7.15 we plot the vorticity distribution on the cylinder surface at $t = 0.2$ and $t = 0.4$ for $Re = 3000$. By comparing these results with the analytical solutions, we find that the body vorticity obtained is satisfactory. Since this measure is directly related to the frictional drag, we guarantee the agreement of the frictional drag with the analytical solution as shown in Figures. 7.12 through 7.14 .

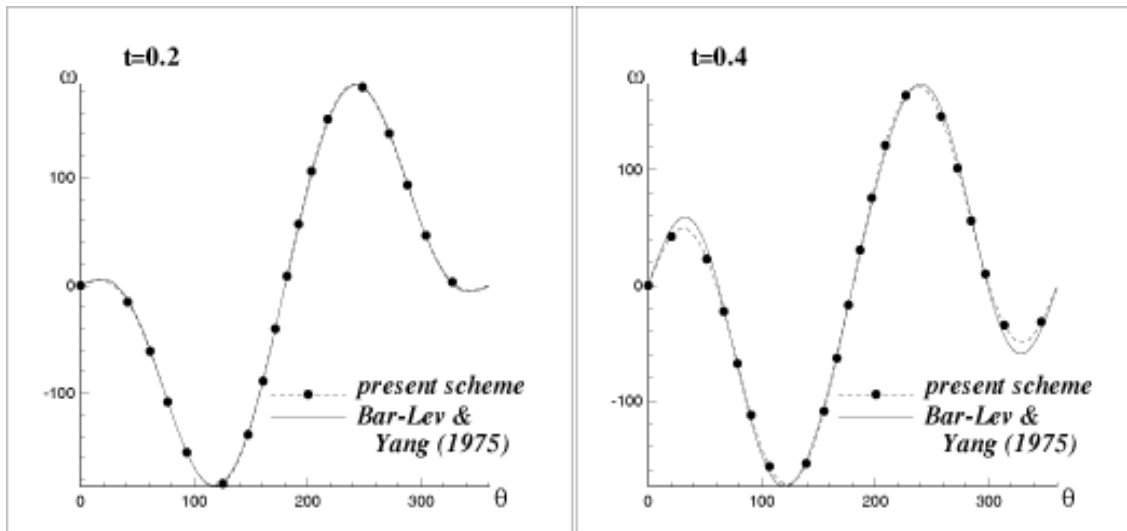


Figure 7.15 Comparison of the computed surface vorticity with the analytical solution of the impulsively started circular cylinder at $Re = 3000$ with the 600×80 grid, $\Delta t = 0.005$ and $R_o = 1.5$.

Figure 7.16 shows the time evolution of the primary separation position for $Re = 9500$. The position is determined in such a way that the body vorticity is zero. The separation angle θ_s is measured from the rear stagnation point. We observe a rapid development of the separation region at about $t = 0.16$ and a reasonable agreement of the present results with those obtained from the analytical solution.

7.4.3.5 Pressure, velocity and vorticity fields

The pressure distribution on the cylinder surface is shown in Figure 7.17 at several instants.

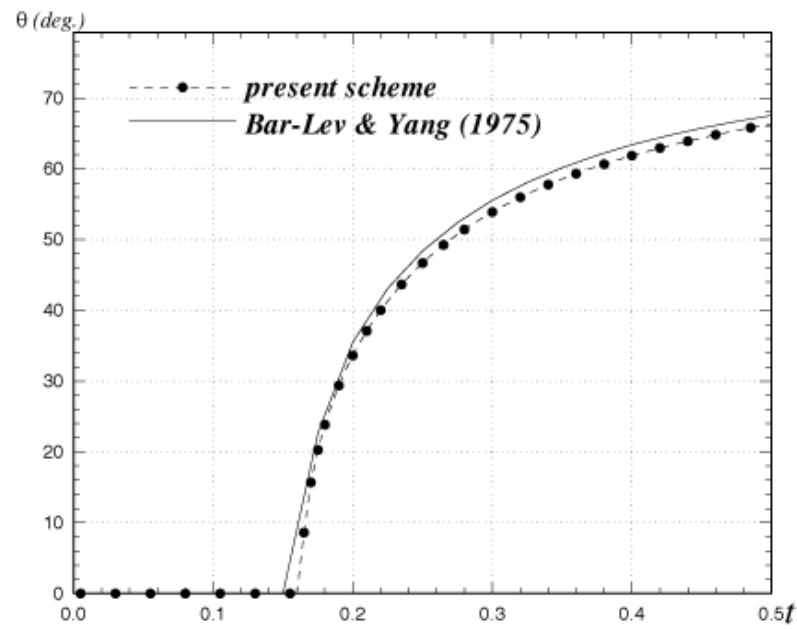


Figure 7.16 Time evolution of the primary separation position of the impulsively started circular cylinder at $Re = 9500$ with $\Delta t = 0.005$, the 600×80 grid and $R_o = 1.5$.

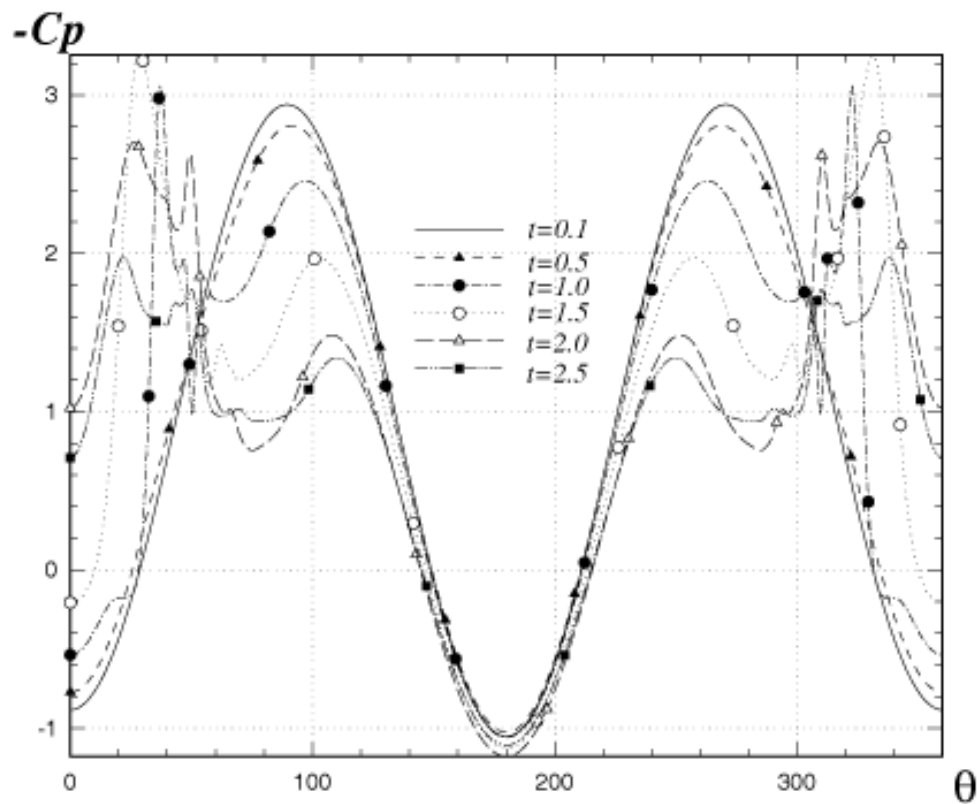


Figure 7.17 Surface pressure distribution of the impulsively started circular cylinder at several

At the early time the pressure distributions represents nearly the distribution obtained from the potential flow analysis, because we can regard a very thin layer of vorticity formed around the cylinder as an equivalent vortex sheet. As this thin layer continues to grow, the pressure distributions are rapidly modified near the strong vortical flow structures. While the change of pressure near the front portion of the cylinder surface is not so great, the pressure distribution near the rear portion is greatly changed. This feature is associated with the complicated flow experimentally observed or numerically simulated in the wake region behind the cylinder at such a high Reynolds number.

Figure 7.18 shows the computed streamline pattern at some instants for $Re = 9500$. Although their results are not presented herein, the pattern reveals good agreement with the experiment by Bouard and Coutanceau (1980) and the computation by Koumoutsakos and Leonard (1995).

In Figure 7.19, the vorticity contours at several instants for $Re = 9500$ are presented. These contours are reasonably compared to other available results (e.g. those in figure 26 in Koumoutsakos and Leonard, 1995). The complicated interaction between the vortical structures developed at the cylinder surface is expected to appear as time advances. This deduction can be also drawn from the corresponding pressure fields shown in Figure 7.20. The strong vortical flow forms a lower pressure region moving downstream and the vorticity strength is slightly weaker by the viscous diffusion as time advances.

The comparison between the time-averaged vorticity flux and the vorticity flux at the end of the time interval is presented in Figure 7.21. It is observed that their difference is negligible except in their high peak value region. The vorticity flux defined in the time-averaged sense when we solved the vorticity transport equation reflects well the global coupling of the vorticity flux with the pressure. However, in the present method, the calculation of the vorticity flux at the end of the time step was separately done because we need the calculation of the pressure drag.

By applying the present numerical algorithm for the impulsively started circular cylinder problems, we have validated the present formulation.

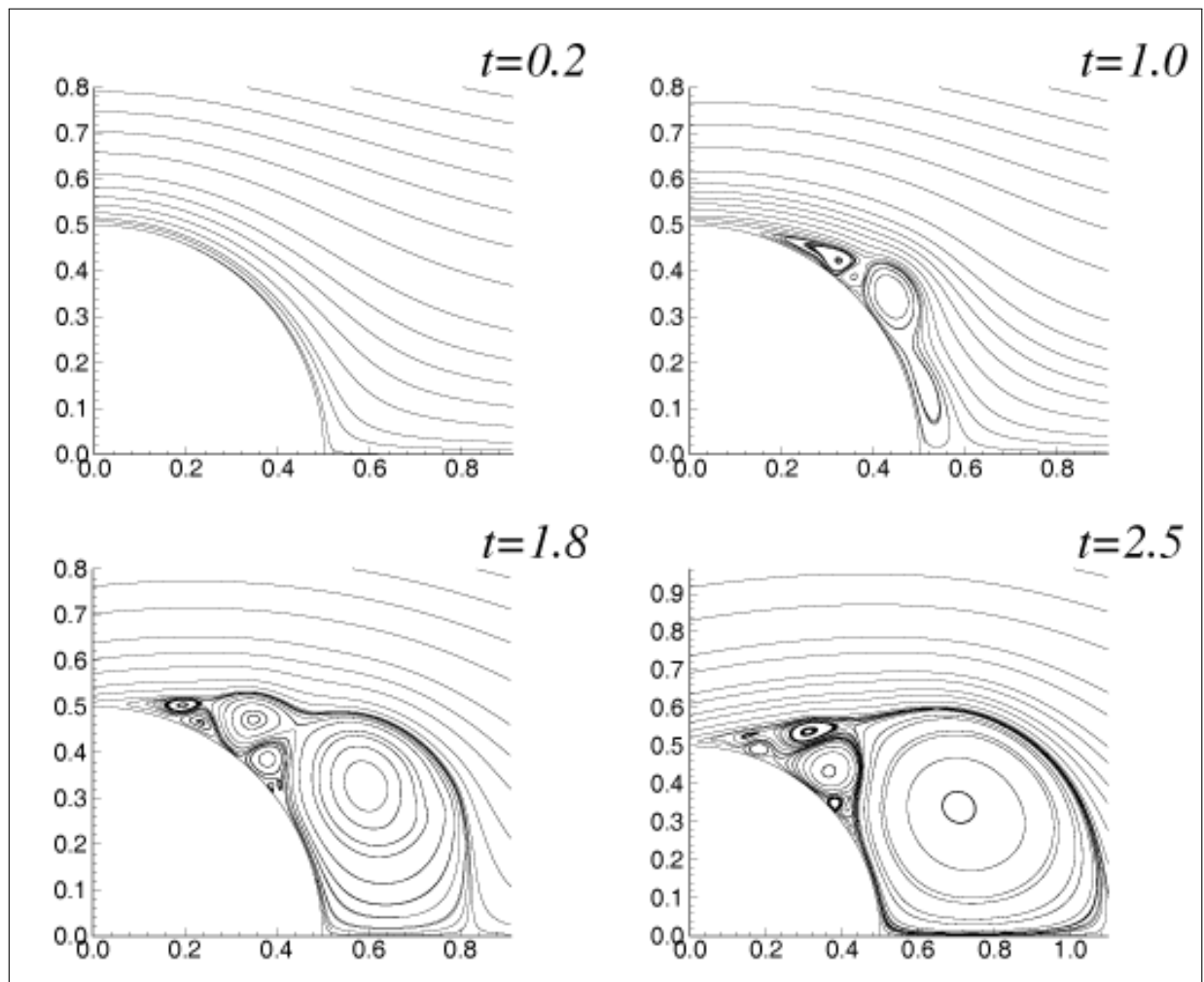


Figure 7.18 Streamline patterns of the impulsively started circular cylinder for $Re = 9500$ with $\Delta t = 0.005$, the 600×80 grid and $R_o = 1.5$.

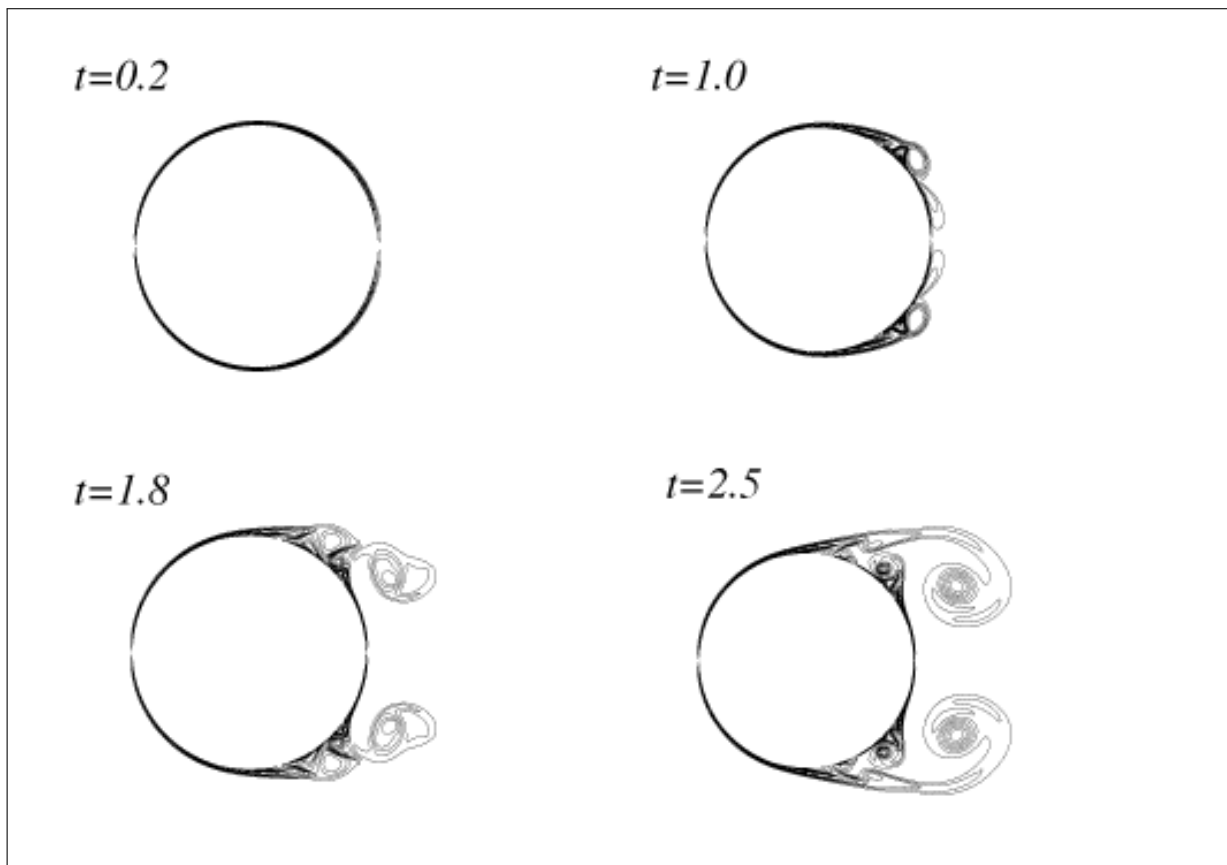


Figure 7.19 Vorticity contours of the impulsively started circular cylinder for $Re = 9500$ with $\Delta t = 0.005$, the 600×80 grid and $R_o = 1.5$.

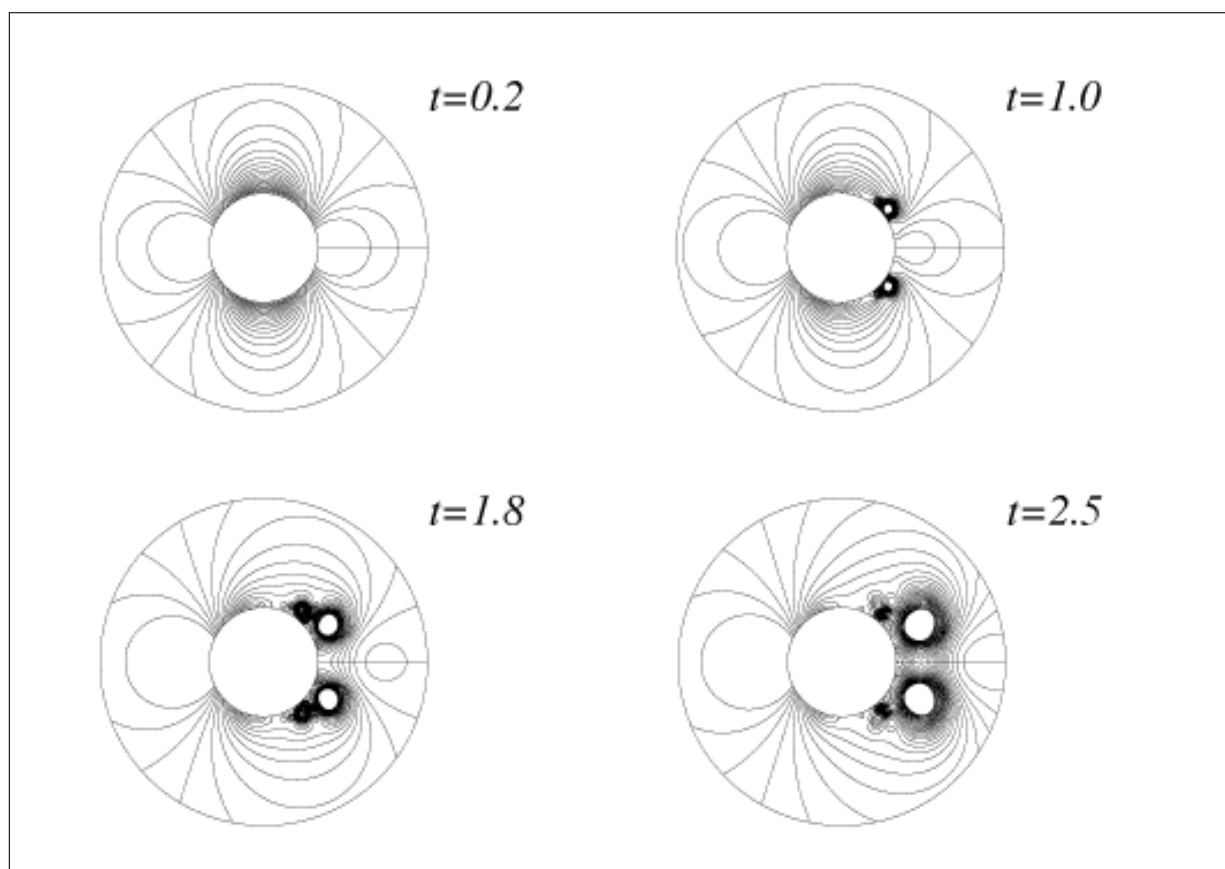


Figure 7.20 Pressure contours of the impulsively started circular cylinder for $Re = 9500$ with $\Delta t = 0.005$, the 600×80 grid and $R_o = 1.5$.

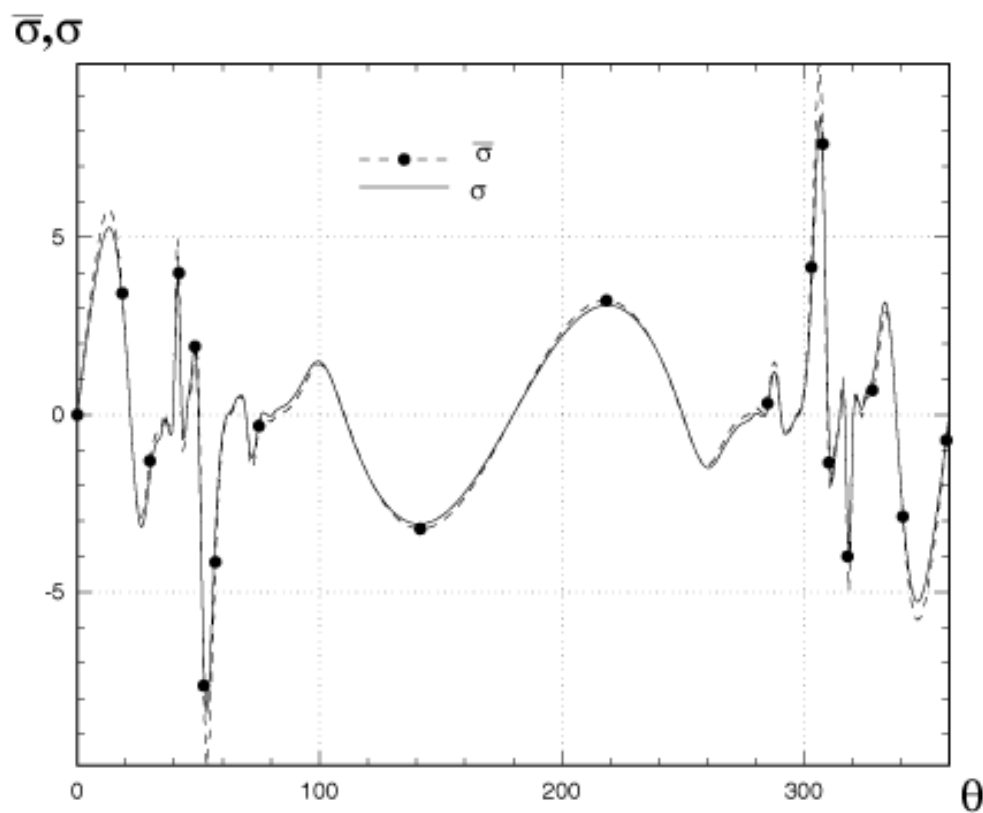


Figure 7.21 Time-averaged vorticity fluxes ($\bar{\sigma}$) of the impulsively started circular cylinder in $t_1 - \Delta t < t < t_1$ and vorticity flux (σ) at $t = t_1$, where $t_1 = 2.5$ for $Re = 9500$ with $\Delta t = 0.005$, the 600×80 grid and $R_o = 1.5$.

7.5 Oscillating Circular Cylinder Problems

7.5.1 Key parameters

The motion of circular cylinders in a fluid at rest is especially of interest in fields of offshore and civil engineering, such as marine risers, subsurface pipelines, etc. An overall review is given by Williamson (1996) and by Sumer and Fredsøe (1997).

When the relative flow past a cylinder is undergoing sinusoidal oscillations, the structure of the flow generated by the cylinder depends mainly on two parameters, namely, the Keulegan-Carpenter number, KC and the Reynolds number, Re . The KC number is defined by

$$KC = \frac{U_m T}{D} = \frac{2\pi A_0}{D} \quad (7.32)$$

in which U_m is the maximum velocity, T is the period of the oscillatory flow, and A_0 is the amplitude of the motion. The Reynolds number is defined as




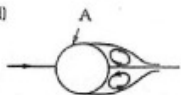


$$Re = \frac{U_m D}{\nu} \quad (7.33)$$

where ν is the kinematic viscosity of the fluid. The ratio

$$\beta = \frac{Re}{KC} = \frac{D^2}{\nu T}, \quad (7.34)$$

being the *Stokes parameter* is a viscous scale parameter (Sarpkaya 1986). Many researchers measured forces acting on a circular cylinder in oscillatory flow as a function of KC and β .

Table 7.1 Regimes of flow around a circular cylinder in oscillatory flow at $Re = 10^3$. Source for $KC < 4$ is from Sarpkaya (1986), and for $KC > 4$ from Williamson (1985).

$KC < 1.1$	a) 	No Separation Creeping flow
$1.1 < KC < 1.6$	b) 	Separation with Kármán vortices
$1.6 < KC < 2.1$	c) 	A pair of symmetric vortices
$2.1 < KC < 4$	d) 	A pair of symmetric vortices Turbulence over the cylinder
$4 < KC < 7$	e) 	A pair of asymmetric vortices
$7 < KC$	f) 	Vortex shedding

7.5.2 Flow characteristics

Investigating the physical meaning of the KC number, the numerator of the right-hand side of the Eq. (7.32) is proportional to the stroke of the motion, namely $2A_0$, while the denominator of the diameter of the cylinder D , represents the width of the cylinder. Small KC numbers therefore mean that the orbital motion of the fluid particles is small relative to the total width of the cylinder. When KC is very small, separation behind the cylinder may not even occur. Large KC numbers imply that the fluid particles travel quite large distance relative to the total width of the cylinder, resulting in separation and probably vortex shedding. For very large KC numbers ($KC \rightarrow \infty$), it is expected that the flow for each half period of the motion resembles that experienced in a steady current (Sumer & Fredsøe 1997).

Experimental investigations of the oscillatory flow around a circular cylinder at small KC have shown that the flow can be classified into a number of different flow regimes governed mainly by KC and with a weak dependency on Re (Bearman *et al.* 1985, Williamson 1985, Sarpkaya 1986). At $KC \ll 1$, the

flow remains symmetrical, attached, and two-dimensional. As KC is increased, the flow becomes asymmetrical ($KC = 4 \sim 5$). At $KC = 10$, a transverse vortex street appears. Table 7.1 summarizes the changes of the flow pattern as the KC number is increased at $Re = 10^3$. Notice that limits of KC regimes are dependent on Re (Justesen 1991, Summer & Fredsøe 1997). By further increasing the KC number, the so-called *vortex-shedding regimes* ($KC > 7$, $Re = 10^3$) appear. According to the description of the vortex trajectory patterns in a systematic manner by Williamson (1985), in the vortex shedding regimes the vortex shedding occurs during the course of each half period of the oscillatory motion. There are several such regimes, each of which has different vortex flow pattern, observed for different ranges of the KC number. These KC ranges include $7 < KC < 15$, $15 < KC < 24$, $24 < KC < 32$, etc.

Figure 7.22 illustrates the time development of vortex motions in the regime at $7 < KC < 15$. The major portion of the KC range, namely $7 < KC < 13$ (Figure 7.22 a), is known as the transverse vortex street regime. The arrows in Figure 7.22 refer to cylinder motion. The wake consists of a series of vortices convecting out to one side of the cylinder in the form of a street. Figure 7.22 b shows the vortex shedding patterns in the regime at $13 < KC < 15$. The wake consists of a series of pairs convecting away each cycle in the direction of about 45° to the flow oscillation direction, from only one side of the cylinder. In Figure 7.22 a and Figure 7.22 b, shown is always one pair of vortices which convect away from the cylinder. It is called “*the single pair regime*”.

Figure 7.23 shows the time development of vortex motions in the case of $15 < KC < 24$, that corresponding to “*double pair regime*”. The resultant wake is due to two vortices shed during each half cycle. Two trails of vortex pairs convect away from the cylinder in opposite directions and from opposite sides of the cylinder.

Figure 7.24 depicts the vortex motions in the case of $24 < KC < 32$, namely “*the three pairs regime*”. The wake of three vortices shed during a half cycle becomes three vortex pairings in a cycle. By varying both β and KC (correspondingly Re), flow patterns may be classified into several regimes according to their structure. The KC and β regimes are plotted in Figure 7.25. Eight regimes are labelled by A* through G based on experimental results by

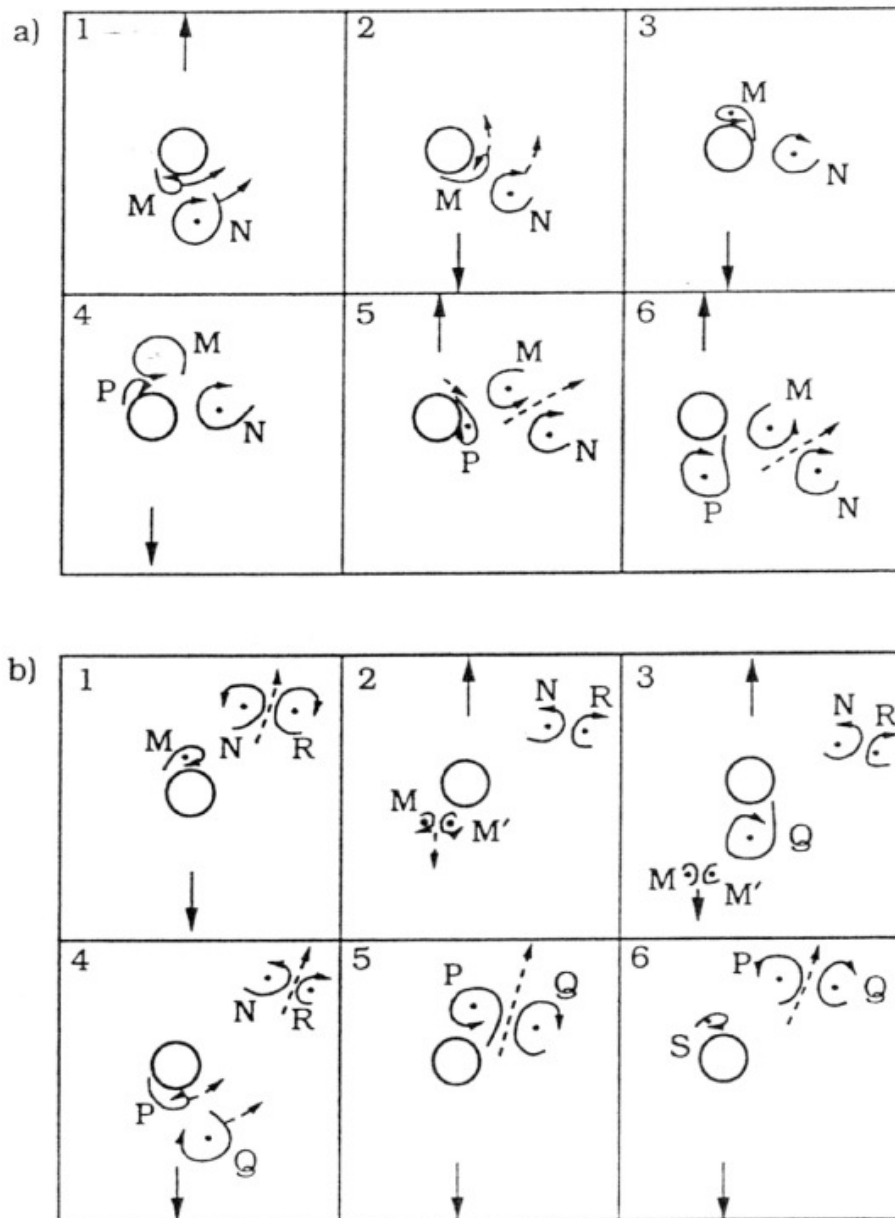


Figure 7.22 Single pair regime of flow around a circular cylinder in oscillatory motion for $7 < KC < 15$. (a) $7 < KC < 13$; (b) $13 < KC < 15$. From Williamson (1985).

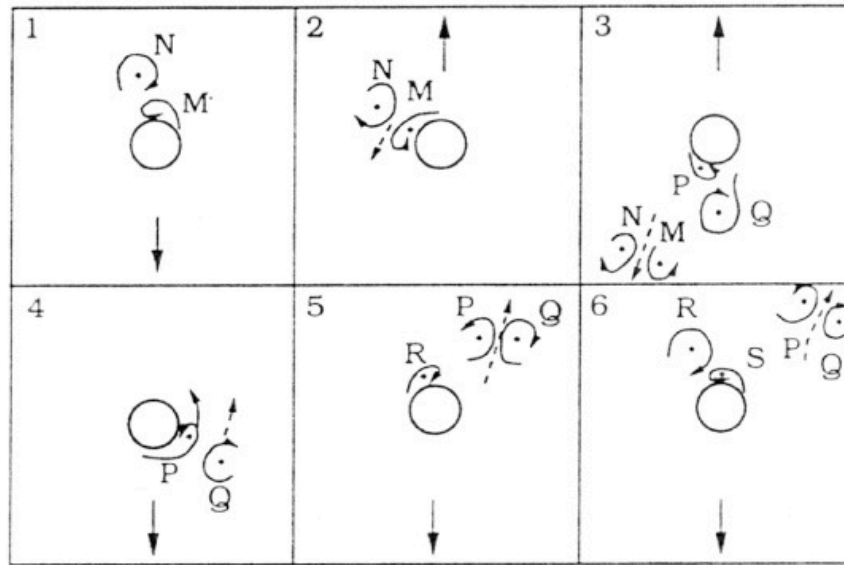


Figure 7.23 Double-pair regime of flow around a circular cylinder in oscillatory motion for $15 < KC < 24$. From Williamson (1985).

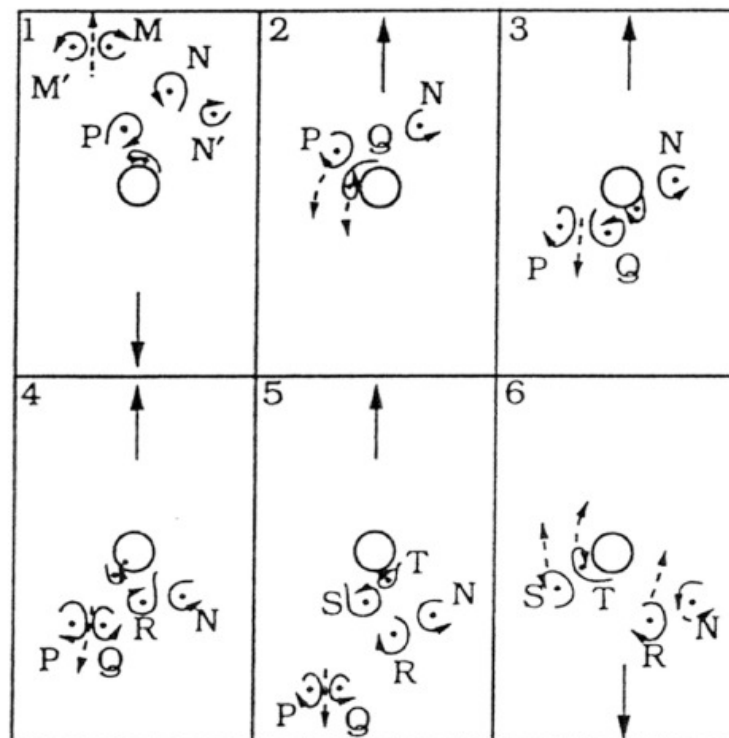


Figure 7.24 Three-pair regime of flow around a circular cylinder in oscillatory motion for $24 < KC < 32$. From Williamson (1985).

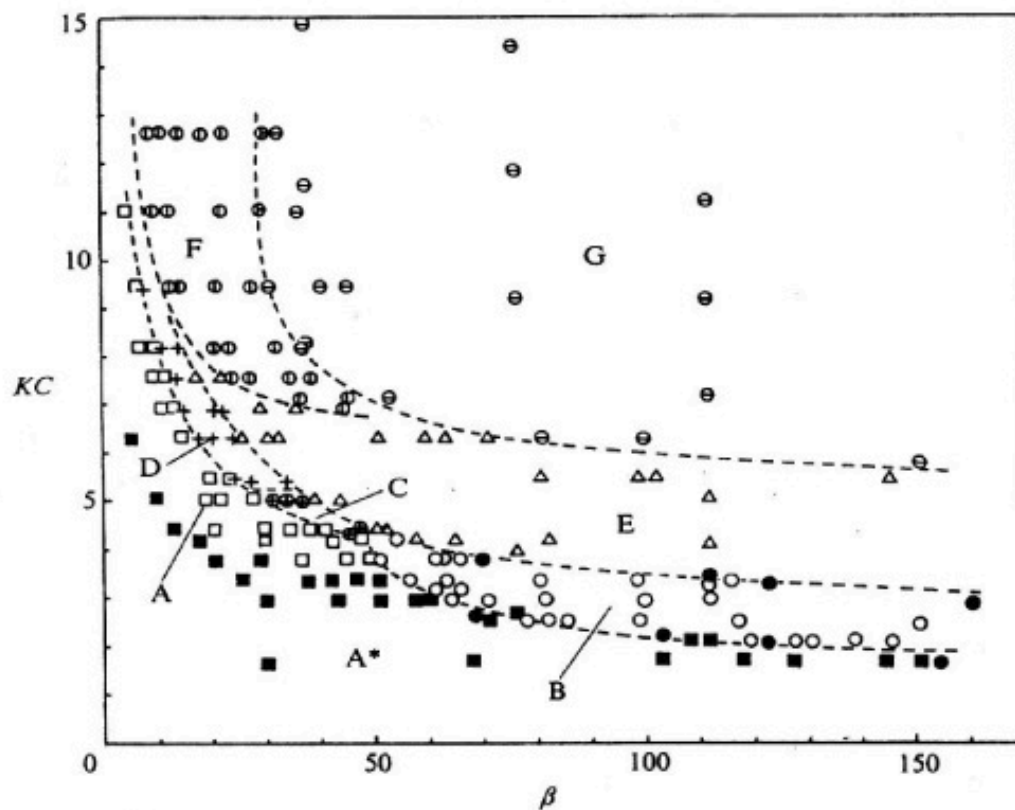


Figure 7.25 Classification of flows around a circular cylinder in oscillatory motion. Flow patterns are identified within eight regimes indicated A* – G. ■, A*; □, A; ○, B; ⊕, C; +, D; △, E; ⊙, F; ⊖, G; ●, critical values for appearance of a streaked flow. From Tatsuno & Bearman (1989).

Tatsuno & Bearman (1989). Principal features of the oscillating flow in the eight regimes are summarized in Table 7.2.

Table 7.2 Principal features of the flows classified in eight regimes of flow around a circular cylinder in oscillatory motion with KC and β . From Tatsuno & Bearman (1989).

flow regimes	principal features
A*	No flow separation; secondary streaming two-dimensional
A	Two vortices shed symmetrically per half cycle two-dimensional
B	Three-dimensional instability longitudinal vortices
C	Rearrangement of large vortices three-dimensional
D	Flow convected obliquely to one side of the axis of oscillation; three-dimensional
E	Irregular switching of flow convection direction three dimensional
F	Flow convected diagonally three dimensional
G	Transverse vortex street three dimensional

Another main feature of the oscillating cylinder is the relation between the vortex shedding frequency and lift frequency. It appears that the peak of the lift force occurs immediately after the reversal motion of the cylinder is associated with the return of the most recently shed vortex to the cylinder, while the other peaks in the lift variation are associated with the vortex shedding. Thus, it is evident that, in oscillatory flows, the lift force frequency is not identical to the vortex shedding frequency (Sumer & Fredsøe 1997). One way for determining lift frequency is by using power spectrum of the lift force and identifying the fundamental frequency. Williamson (1985)'s work, where the ratio of Re to KC was kept constant at $\beta = Re/KC \approx 255$ in one series of the experiments and at $\beta \approx 730$ in the other, has indicated that the fundamental lift frequency increases with increasing KC , as shown in Table 7.3.

Table 7.3 Fundamental lift frequencies of the observed flow around a circular cylinder in oscillatory motion. From Williamson (1985).

KC regime	KC regime	Reynolds number Re	Normalized fundamental lift frequency (= Number of oscillation in the lift per flow-cycle) $N_L = \frac{f_L}{f_\omega}$
Single pair	$7 < KC < 15$	$1.8 - 3.8 \times 10^3$	2
Double pair	$15 < KC < 24$	$3.8 - 6.1 \times 10^3$	3
Three pairs	$24 < KC < 32$	$6.1 - 8.2 \times 10^3$	4
Four pairs	$32 < KC < 40$	$8.2 - 10 \times 10^3$	5

7.5.3 Formulation for moving frame fixed to cylinder

The present calculation provides solutions obtained by the Eulerian FVM method for the problem of the oscillating cylinder. It is expected to provide the simulations of vortex shedding from the cylinder. In addition, when investigating the characteristic of lift frequency, the vortex shedding frequencies are investigated with the variety of the flow regimes with each other KC and β .

Let us consider the harmonic in-line motion of the cylinder in a fluid at rest. Position, velocity and acceleration of the local moving coordinate at the center of the circular cylinder are defined, respectively, as

$$\underline{x} = A_0 \sin(f t) \underline{i}, \quad (7.35)$$

$$\underline{\dot{x}} = \underline{q}_F = A_0 f \cos(f t) \underline{i}, \quad (7.36)$$

$$\underline{\dot{q}}_F = -A_0 f^2 \sin(f t) \underline{i}. \quad (7.37)$$

The relative velocity to the local moving frame is $\underline{q} = -\underline{q}_F + \underline{u}$ where \underline{u} is the velocity in the inertia frame. Assume the acceleration of the local moving frame is not zero, then Navier- Stokes equation at the local moving frame is represented as

$$\frac{D\underline{q}}{Dt} + \underline{\dot{q}}_F = -\nabla \left(\frac{p}{\rho} \right) - \nabla \times (\nu \underline{\omega}) \quad (7.38)$$

Vorticity transport equation and pressure equation derived from Eq. (7.38) are not changed at the local moving frame. The vorticity-velocity relation with the Biot-Savart integral(Eq. (6.43)), however, should be included with the velocity on the local moving frame. Dynamic vorticity boundary condition and pressure boundary condition (Eqs. (6.48) through (6.49)), are modified.

The main parameters are non-dimensionalized as

$$Re = \frac{U_0 D}{\nu}, \quad t^* = \frac{U_0 t}{D}, \quad U_0 = A_0 f, \quad KC = \frac{2\pi A_0}{D} \quad (7.39)$$

where U_0 is the maximum velocity, D is cylinder diameter, and A_0 is the amplitude of the cylinder. With the non-dimension parameters, the governing equations are expressed as

$$\frac{\partial \omega}{\partial t} + \nabla \cdot (\underline{q} \omega) = \frac{1}{Re} \nabla^2 \omega, \quad (7.40)$$

$$\underline{q} = -\underline{U}_0 \cos\left(\frac{2\pi}{KC} t^*\right) \underline{i} + \oint_C (\omega \underline{k}) \times \nabla G dl. \quad (7.41)$$

$$\nabla^2 \left(\frac{1}{2} \underline{q}^2 + \frac{p}{\rho} \right) = \nabla \cdot (\underline{q} \times \omega \underline{k}), \quad (7.42)$$

These equations are equivalent to Eqs. (6.42) through (6.44). The boundary conditions of vorticity and pressure with no-slip condition are

$$\frac{1}{Re} \frac{\partial \omega}{\partial n} \underline{k} = \underline{n} \times \left\{ \left(\frac{D\underline{q}}{Dt} + \nabla p \right) - \frac{2\pi}{KC} \sin\left(\frac{2\pi}{KC} t^*\right) \underline{i} \right\} \quad (7.43)$$

$$\frac{\partial H}{\partial n} = \underline{n} \cdot \left\{ \left(\underline{q} \times \omega \underline{k} - \frac{1}{Re} \nabla \times \omega \underline{k} \right) + \frac{2\pi}{KC} \sin\left(\frac{2\pi}{KC} t^*\right) \underline{i} \right\} \quad (7.44)$$

These are comparable to Eqs. (6.48) and (6.49). (See also Kim *et al.* (2003).)

7.5.4 Numerical simulation

The calculation for three different conditions of KC and β is performed, each of which is characterized with the different flow regimes.

7.5.4.1 Case 1: $KC = 7, \beta = 143$ ($Re = 1000$)

According to Tatsuno and Bearman (1989), the regime of the present parameters ($KC = 7, \beta = 143$) is the regime named G, as shown in Figure 7.25 and Table 7.2. The principal feature in this regime has transverse vortex street, i.e., the vortex is shedding in direction perpendicular to the in-line motion of the cylinder. The feature of vortex shedding by the present calculation is shown in Figure 7.26.

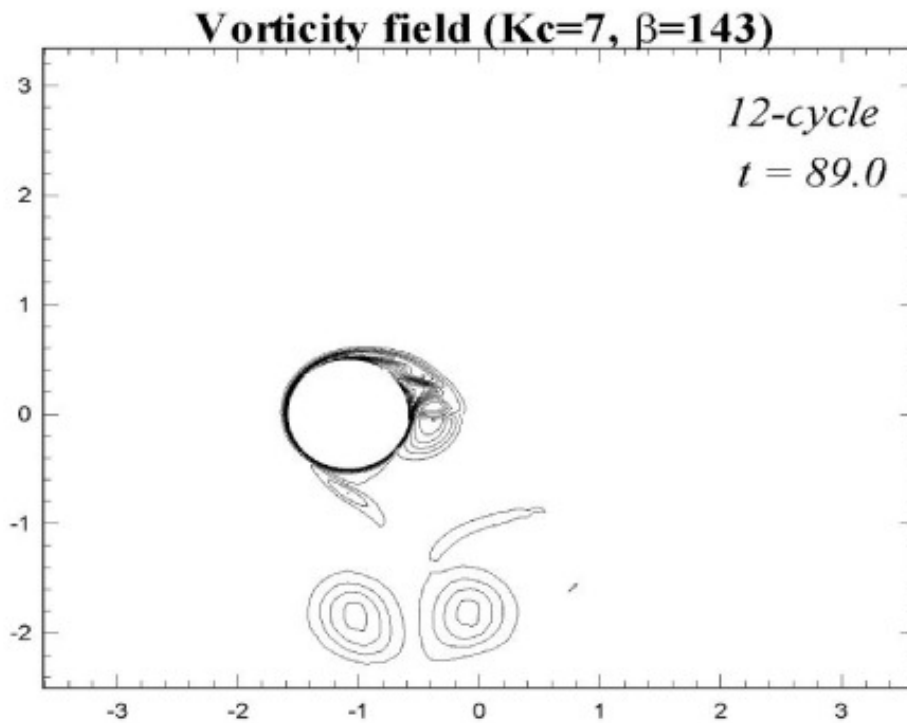


Figure 7.26 Transverse vortex street pattern of flow around a circular cylinder in oscillatory motion at $T = 89$ for $KC = 7, \beta = 143$.

In this figure, the single vortex pair is captured at time $t = 89$. The single vortex pair is convecting out perpendicular to one side of the cylinder. This result shows a good agreement with the flow pattern of the regime named G.

Figure 7.27 represents the time history of drag and lift coefficients. In order to analyze the periodic physics of the drag and lift forces, the time domain is converted into the frequency domain by the Fourier transformation.

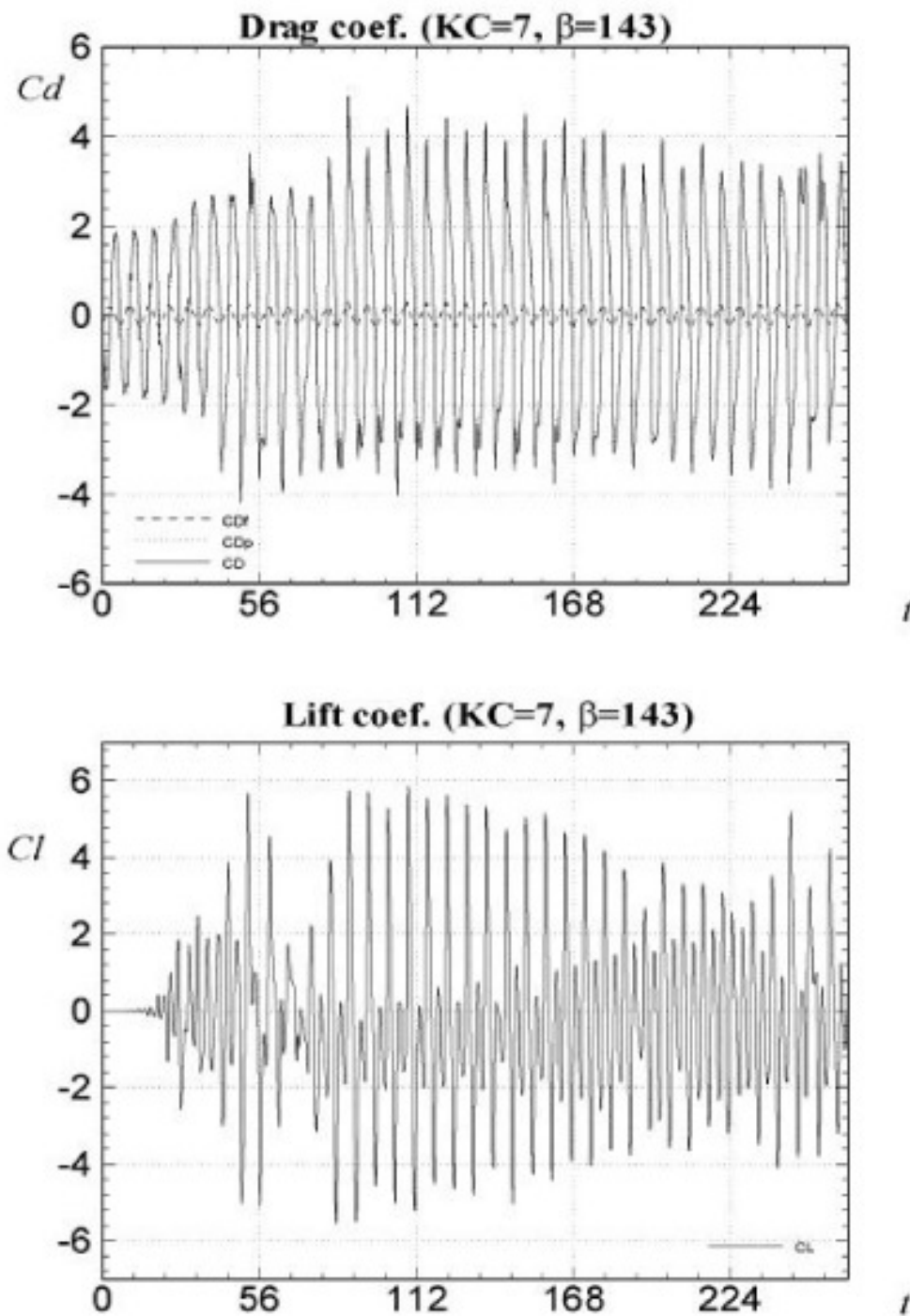


Figure 7.27 Time history of drag and lift forces of flow around a circular cylinder in oscillatory motion for $KC = 7$, $\beta = 143$.

As shown in Figure 7.28, the peak of drag forces in frequency domain occurs only once at $\omega \approx 0.92$.

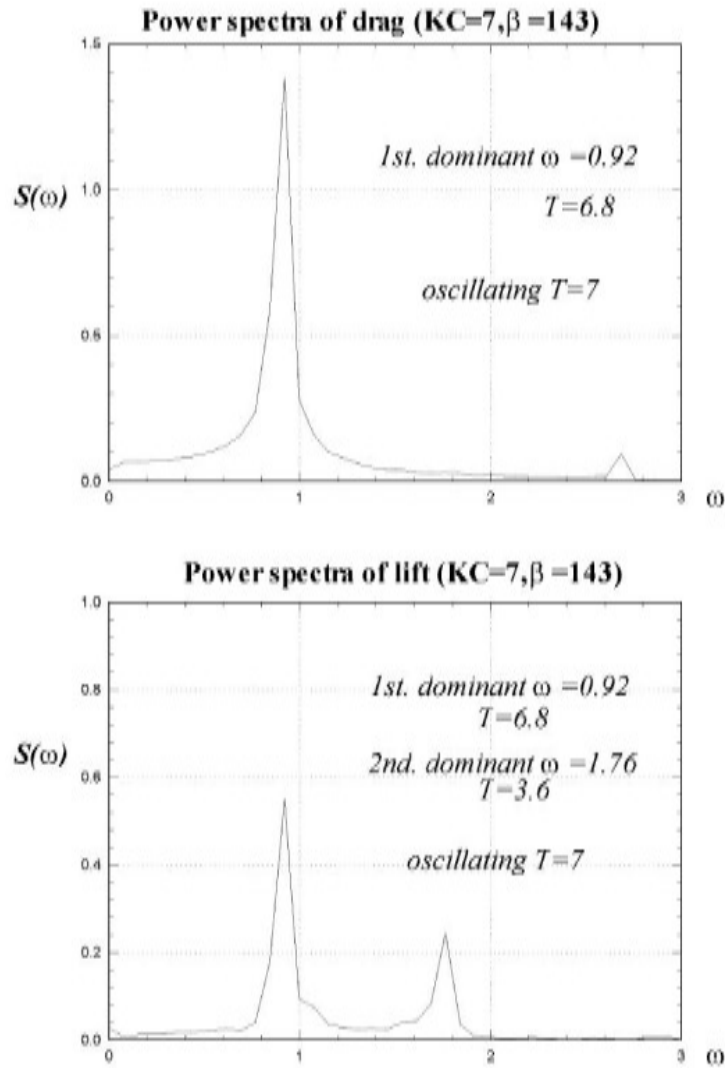


Figure 7.28 Power spectra of drag and lift forces of flow around a circular cylinder in oscillatory motion for $KC = 7$, $\beta = 143$.

The time cycle of cylinder motion is about 7, and the dominant time cycle of drag force shown in Figure 7.28 is about 6.8. The cycle of drag force coincides with the cycle of motion. On the other hand, the peaks of lift forces in frequency are appeared twice. The first fundamental frequency is $\omega = 0.92$ and the second one is $\omega = 1.76$, which corresponding to $T = 6.8$ and $T = 3.6$, respectively. The maximum lift force is appeared twice during one cycle motion of the cylinder. This fact coincides with the characteristic of the fundamental lift frequency observed by other researchers which is described with Table 7.3 in the previous section.

7.5.4.2 Case 2: $KC = 10, \beta = 20$ ($Re = 200$)

In Figure 7.25 and Table 7.2, the regime of the present parameters ($KC = 10, \beta = 20$) corresponds to F. The principal feature in this regime is the flow convected diagonally, i.e., when the cylinder moves from right to left, a large clockwise vortex is formed on the upper side of the cylinder and a smaller counter-clockwise vortex on the lower side of the cylinder. As the clockwise vortex becomes stronger, a transverse flow appears behind the two vortices. When the cylinder reverses, the stronger clockwise vortex is convected back to the cylinder which induces a new vortex. The transverse flow developed behind the cylinder distorts the trail of flow away from the oscillation axis. This causes one vortex pair of diagonal pattern to shed. In the half cycle from left to right, a strong clockwise vortex and a flow crossing the axis of oscillation are developed in the same manner as in the previous half cycle.

Figure 7.29 shows diagonally pattern formed by single-pair vortex. This result shows a good agreement with the flow pattern of the regime named F. Figure 7.30 shows the time history of drag coefficient and lift coefficient. In

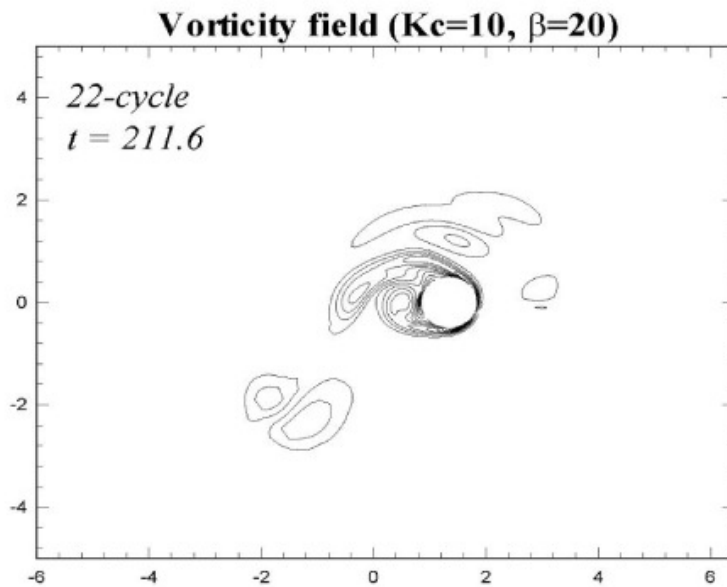


Figure 7.29 Diagonally convected single-pair vortex pattern of flow around a circular cylinder in oscillatory motion at $T = 211.6$ for $KC = 10, \beta = 20$.

Figure 7.31, the peak of drag forces in frequency domain is seen to appear only

once at $\omega \approx 0.61$.

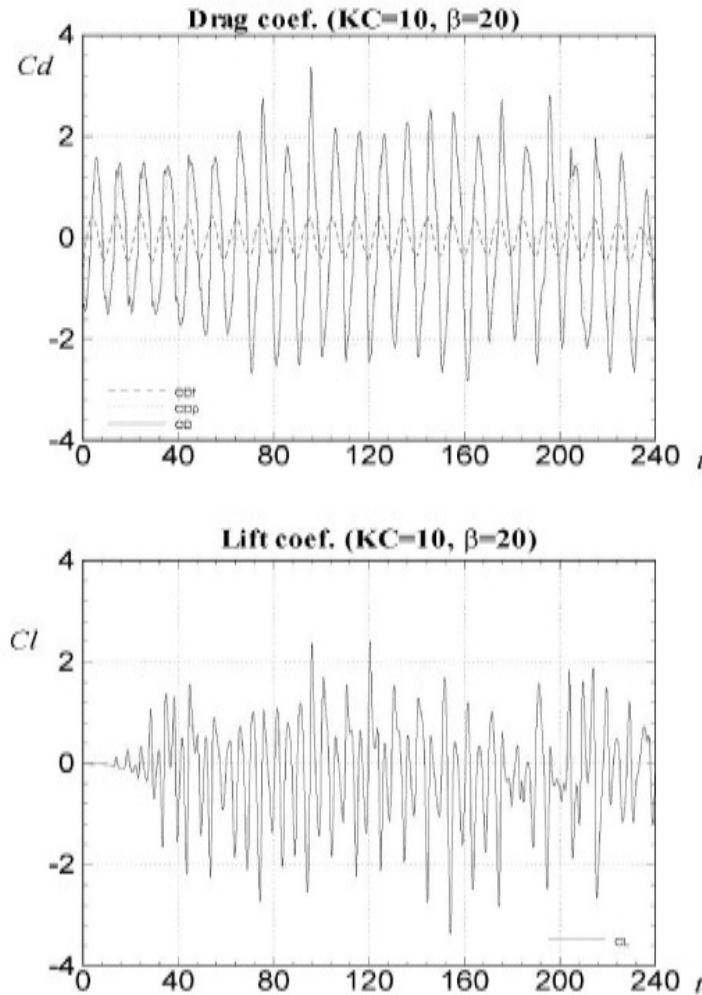


Figure 7.30 Time history of drag and lift forces of flow around a circular cylinder in oscillatory motion at $T = 211.6$ for $KC = 10$, $\beta = 20$.

The time cycle of cylinder motion is about 10, and the dominant time cycle of drag force observed in Figure 7.31 is about 10.3. The cycle of drag force coincides with the cycle of motion. The peak of lift forces in frequency is seen to appear only once. However, the dominant frequency is $\omega = 1.23$, which means that the dominant time cycle of lift force is $T = 5.1$. The maximum lift force is appeared twice during one cycle motion of the cylinder. This fact coincides with the characteristics of the fundamental lift frequency observed by other researchers (Table 7.3).

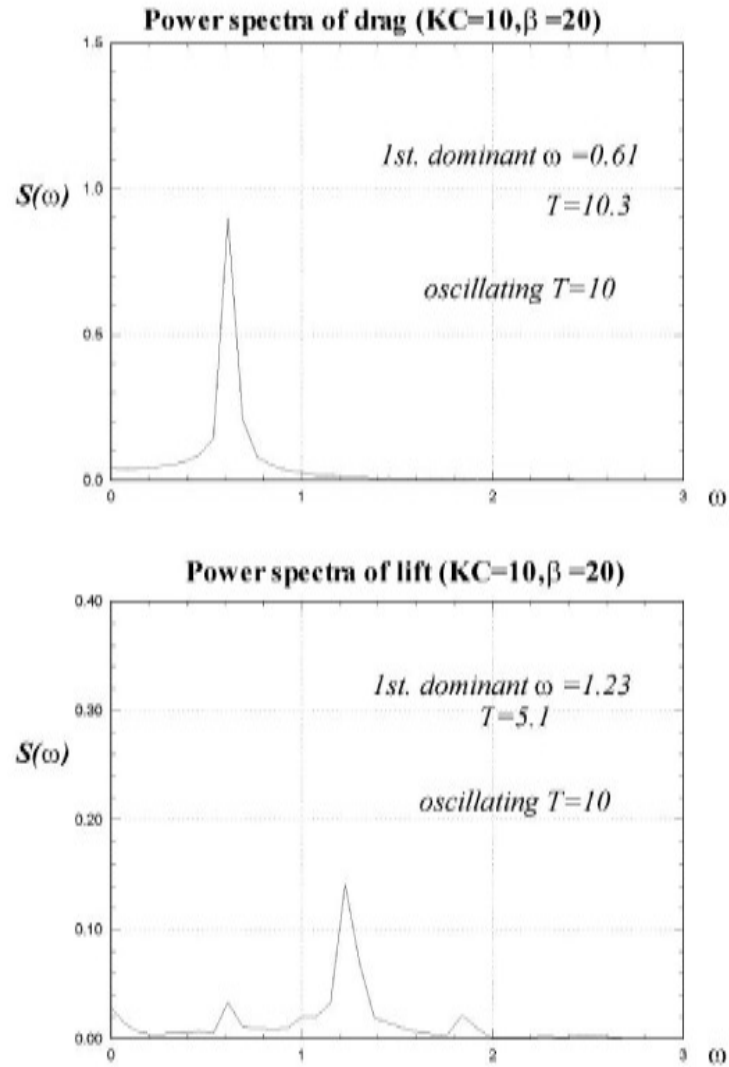


Figure 7.31 Power spectra of drag and lift forces of flow around a circular cylinder in oscillatory motion for $KC = 10$, $\beta = 20$.

7.5.4.3 Case 3: $KC = 16, \beta = 62.5$ ($Re = 1000$)

In this case, the vortex shedding mechanism is similar to one in the previous cases, but the resulting flow around the oscillating cylinder is more complex due to the larger KC . According to Williamson (1985)(Table 7.1), the remarkable feature of the flow is that double-pair vortex is shedding. The regime of the present parameters is between the regime F and the regime G as shown in Figure 7.25. This regime appears to be similar to the transverse vortex street, but the direction of the flow may change intermittently, into longitudinal, oblique, and transverse direction.

Figure 7.32 shows irregular switching of flow convection pattern formed by double-pair vortex. Figure 7.33 shows the time history of drag coefficient and lift coefficient. With the Fourier transformation, the results are shown in Figure 7.34. In this figure, the peak of drag forces in frequency domain appears once at $\omega \approx 0.38$. The time cycle of cylinder motion is about 16, and the dominant time cycle of drag force in Figure 7.34 is about 16.5. The cycle of drag force coincides with the cycle of motion. The peak of lift forces in frequency appears once. The fundamental frequency is $\omega = 1.15$, namely, the dominant time cycle of lift force is $T = 5.46$. The maximum lift force appears three times in one cycle motion of the cylinder. This fact coincides with the characteristics of the fundamental lift frequency (see Table 7.3).

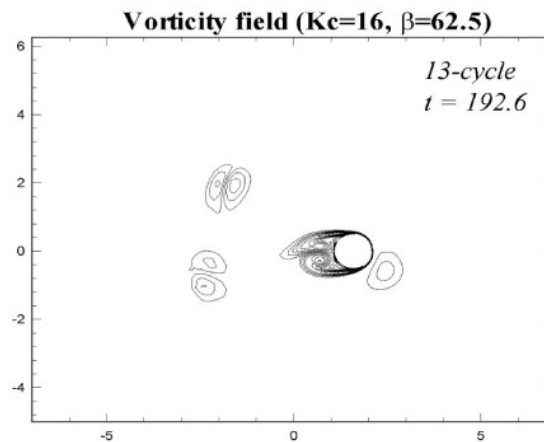


Figure 7.32 Double-pair vortex convection pattern of flow around a circular cylinder in oscillatory motion at $T = 192.6$ for $KC = 16, \beta = 62.5$.

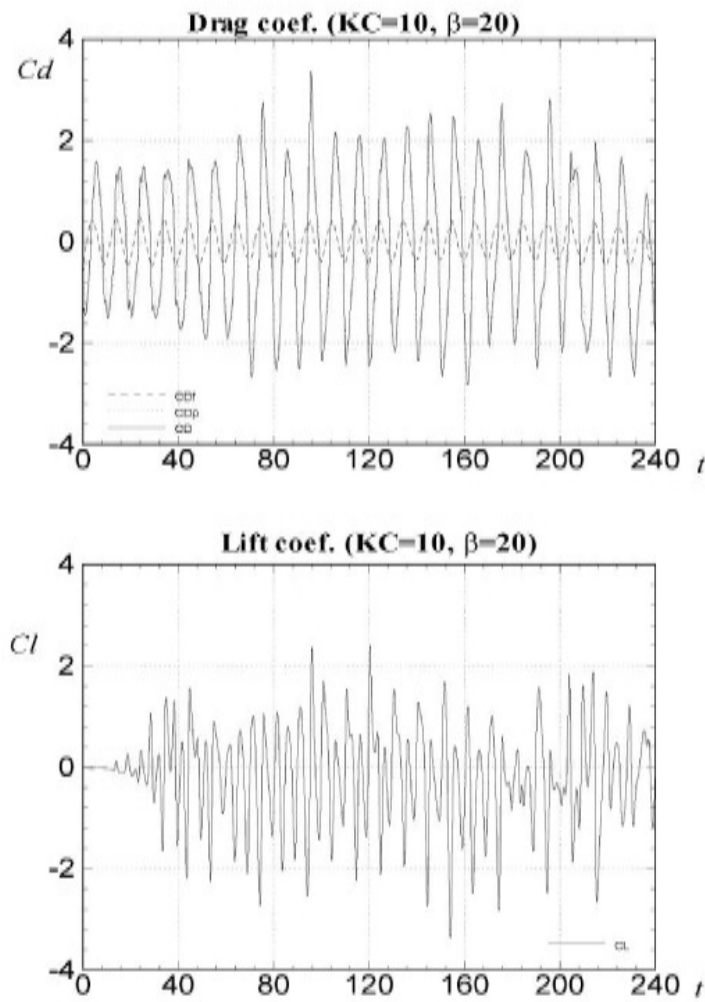


Figure 7.33 Time history of drag and lift forces of flow around a circular cylinder in oscillatory motion for $KC = 16$, $\beta = 62.5$.

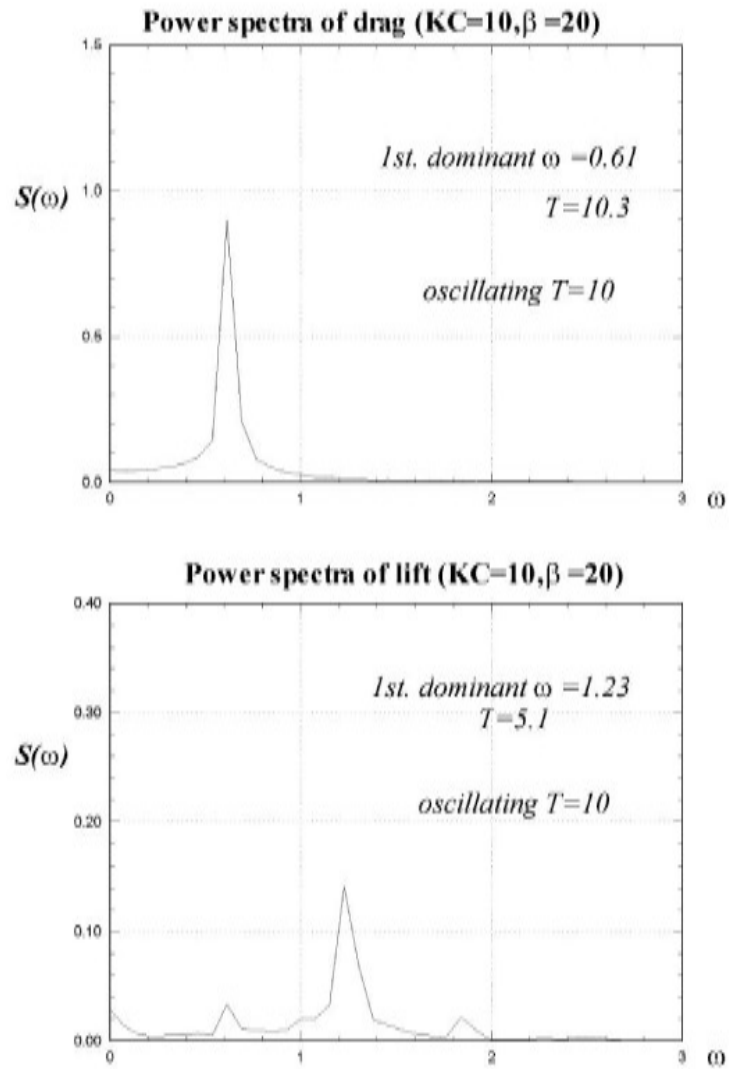


Figure 7.34 Power spectra of drag and lift forces of flow around a circular cylinder in oscillatory motion for $KC = 16$, $\beta = 62.5$.

